Coupling the photospheric and coronal magnetic fields : observations and analysis
by Brian Neal Handy

A thesis submitted in partial fulfillment of the requirements for the degree of Doctor of Philosophy in Physics
Montana State University

Abstract:
The work presented in this thesis is composed of two complementary fields in solar physics. The first section is devoted to current issues in instrument hardware, in particular the Ultraviolet (UV) channel of the Transition Region and Coronal Explorer (TRACE) instrument. The chapter as presented is reproduced from Handy et al. (1998). The TRACE instrument carries UV optics to image solar plasmas in the Lyα &lamba; 1216 Å emission line, the C IV A 1550 Å resonance line doublet, the UV continuum at 1600 Å and a “white light” image centered at ≈ 5000 Å The C IV lines are particularly difficult to image properly as they are superimposed on a background UV continuum that increases six orders of magnitude over the wavelength range 1300-2100 Å Chapter 2 considers the problem of isolating the C IV resonance lines from the UV continuum, discusses the optics used to achieve this goal, presents a formalism for data analysis and finally shows a sample dataset from post-launch observations.

Chapter 3 considers observations from a high time-cadence joint observing cam-paign with the Extreme-ultraviolet Imaging Telescope (EIT, Delaboudiniere et al. 1995) and the Michelsen Doppler Imager (MDI, Scherrer et al. 1995) on the Solar and Heliospheric Observatory (SOHO, Domingo, Fleck, & Poland 1995), 10-14 Au-gust 1997. This coordinated observation makes it possible to observe the response of the (1 MK) solar corona to the evolution of the photospheric magnetic field. Qualita-tive observations show that coronal loops evolve continually on a discontinuous basis: small emerging loops spread, the magnetic footpoints coalesce (or cancel) with other flux concentrations, then the coronal loops reconnect to larger concentrations at a greater range of distances. We find that the quiet solar corona has a typical evolution time scale of nominally 15 hours, in very good agreement with the observations of Schrijver et al. (1997) who find that photospheric magnetic flux concentrations have a lifetime of less than 40 hours. Hence, pairs of flux concentrations must evolve on a timescale of less than 20 hours. We also evaluate two theories of coronal heating via magnetic reconnection and attempt to reconcile our observations against these theoretical predictions.

COUPLING THE PHOTOSPHERIC AND CORONAL MAGNETIC FIELDS: OBSERVATIONS AND ANALYSIS

by

Brian Neal Handy

A thesis submitted in partial fulfillment
of the requirements for the degree

of

Doctor of Philosophy

in

Physics

MONTANA STATE UNIVERSITY — BOZEMAN
Bozeman, Montana

June 1998

APPROVAL

of a thesis submitted by

Brian Neal Handy

This thesis has been read by each member of the thesis committee, and has been found to be satisfactory regarding content, English usage, format, citations, bibliographic style and consistency, and is ready for submission to the College of Graduate Studies.

Loren W. Acton, Ph. D. — Loren W. Acton (Signature) — 7-14-98 Date

Approved for the Department of Physics

John C. Hermanson, Ph. D. — J Herm (Signature) — 7-14-98 Date

Approved for the College of Graduate Studies

Joseph J. Fedock, Ph. D. — Joseph J. Fedock (Signature) — 7/17/98 Date

STATEMENT OF PERMISSION TO USE

In presenting this thesis in partial fulfillment of the requirements for a doctoral degree at Montana State University — Bozeman, I agree that the Library shall make it available to borrowers under rules of the Library. I further agree that copying of this thesis is allowable only for scholarly purposes, consistent with "fair use" as prescribed in the U. S. Copyright Law. Requests for extensive copying or reproduction of this thesis should be referred to University Microfilms International, 300 North Zeeb Road, Ann Arbor, Michigan, 48106, to whom I have granted "the exclusive right to reproduce and distribute my dissertation in and from microform along with the non-exclusive right to reproduce and distribute my abstract in any format in whole or in part."

Signature Brian Harry

Date July 14, 1998

ACKNOWLEDGEMENTS

No work of this magnitude is ever done in a vacuum, and this project was no exception. Space constraints prevent me from properly naming names and placing blame where it is most richly deserved, but a number of people must be fingered:

At Montana State University, thanks go to Loren Acton who took me under his wing as his first graduate student in the newly-formed Solar Physics Group. I'm also grateful for the friendship of several fellow graduate students: Matt Egloff, Michelle Larson, Shane Larson, Gregg Switzer, Tsunefumi Tanaka, Brett Taylor and Mark Weber.

At the Lockheed-Martin Advanced Technology center, a richly-deserved thank you is extended to Ted Tarbell, who provided the voice of reason for the TRACE UV work; Karel Shrijver, my mentor for the latter half of this thesis; Bruce Jurcevich, who taught me to write boilerplate; Tom Pope, who let me hold the screwdriver. I also thank Jake Wolfson, who set the standard for leading a hardware project; Tom Metcalf, who taught me most of what I know about the sun's magnetic field; James Lemen and Marilyn Bruner, who provided guidance along the way. Lastly, thanks also go to David Alexander, Dave Akin, Tom Berger, Chris Edwards, Craig Feinstein, Mandy Hagenaar, Chris Heck, Gary Linford, Mons Morrison, Susan Morrison, Tim Roethig, Greg Slater, Larry Springer, Bob Stern and Jean-Pierre Wülser.

I would also like to acknowledge the hospitality of the folks at the Smithsonian Astrophysical Observatory: Jay Bookbinder, Ed DeLuca, Leon Golub and Rebecca McMullen. Also in that part of the world I thank the folks at Acton Research Corporation: Glen Callahan, Bruce Flint, Scott Flint, Michael LaForge, Joe Oliver and Renee Zajon, who collectively taught me most of what I know about the nature of ultraviolet optics.

This research was sponsored in part by contract NAS5-38099 with NASA Goddard Space Flight Center. I thank Paal Brekke and the HRTS team for providing the data that made the TRACE optical design analysis possible, and the EIT and MDI/SOI teams for their invaluable assistance accessing and reducing the coronal data and magnetogram data used in the latter part of this thesis. I am grateful for accommodation as a graduate study scientist with the Lockheed Martin Solar & Astrophysics Group during the preparation of the TRACE instrument and this paper.

SOHO is a mission of international cooperation between the European Space Agency and the National Aeronautics and Space Administration.

TABLE OF CONTENTS

LIST OF TABLES

LIST OF FIGURES

ABSTRACT

The work presented in this thesis is composed of two complementary fields in solar physics. The first section is devoted to current issues in instrument hardware, in particular the Ultraviolet (UV) channel of the *Transition Region and Coronal Explorer* (TRACE) instrument. The chapter as presented is reproduced from Handy et al. (1998). The TRACE instrument carries UV optics to image solar plasmas in the Lyα λ 1216 Å emission line, the C IV λ 1550 Å resonance line doublet, the UV continuum at 1600 Å and a "white light" image centered at $\approx$ 5000 Å. The C IV lines are particularly difficult to image properly as they are superimposed on a background UV continuum that increases six orders of magnitude over the wavelength range 1300–2100 Å. Chapter 2 considers the problem of isolating the C IV resonance lines from the UV continuum, discusses the optics used to achieve this goal, presents a formalism for data analysis and finally shows a sample dataset from post-launch observations.

Chapter 3 considers observations from a high time-cadence joint observing campaign with the Extreme-ultraviolet Imaging Telescope (EIT, Delaboudinière et al. 1995) and the Michelsen Doppler Imager (MDI, Scherrer et al. 1995) on the Solar and Heliospheric Observatory (SOHO, Domingo, Fleck, & Poland 1995), 10–14 August 1997. This coordinated observation makes it possible to observe the response of the (1 MK) solar corona to the evolution of the photospheric magnetic field. Qualitative observations show that coronal loops evolve continually on a discontinuous basis: small emerging loops spread, the magnetic footpoints coalesce (or cancel) with other flux concentrations, then the coronal loops reconnect to larger concentrations at a greater range of distances. We find that the quiet solar corona has a typical evolution time scale of nominally 15 hours, in very good agreement with the observations of Schrijver et al. (1997) who find that photospheric magnetic flux concentrations have a lifetime of less than 40 hours. Hence, *pairs* of flux concentrations must evolve on a timescale of less than 20 hours. We also evaluate two theories of coronal heating via magnetic reconnection and attempt to reconcile our observations against these theoretical predictions.

CHAPTER 1

INTRODUCTION

The work presented in this thesis is composed of two complementary fields in solar physics. Chapter 2 is devoted to current issues in instrument hardware, in particular the Ultraviolet (UV) channel of the *Transition Region and Coronal Explorer* (TRACE) instrument. The chapter as presented is reproduced from Handy et al. (1998). Chapter 3 considers observations and results from a high cadence joint observing campaign with the Extreme-ultraviolet Imaging Telescope (EIT, Delaboudinière et al. 1995) and the Michelsen Doppler Imager (MDI, Scherrer et al. 1995) on the Solar and Heliospheric Observatory (SOHO, Domingo et al. 1995), 10-14 August 1997. TRACE is similar in design and capability to the EIT instrument, with greater temporal and spatial resolution over a smaller field of view.

1.1 The Transition Region.

The solar transition region represents the layer between the relatively cool ($\simeq 10^4$ K), optically thick chromosphere and the hot ($\simeq 10^6$ K), tenuous, optically thin solar corona. This shift in temperature T (and hence density ρ, as the pressure P must be continuous across the boundary and $P \sim \rho T$) occurs so rapidly that the transition region more accurately represents a temperature regime instead of a geometric layer (Stix 1989). Observations (both filtergrams and spectral observations) of transition region emission lines show a very inhomogeneous environment with a great deal of structure (Reeves, Noyes, & Withbroe 1972; Brueckner 1981; Damè et al. 1996). Figure 1.1 represents an idealized (stratified, spherically symmetric) model of the solar atmosphere that demonstrates this sharp discontinuity in the physical parameters in that region.

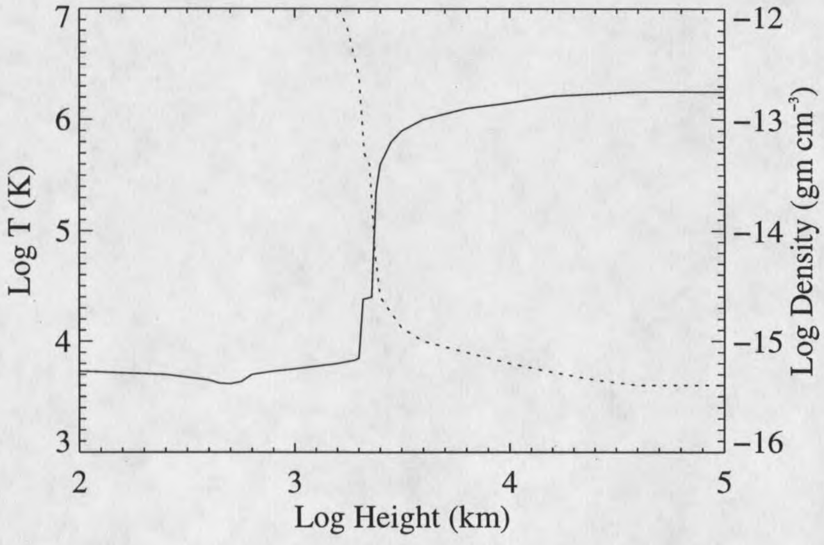

Figure 1.1: Average temperature and density gradients in the solar atmosphere. This model represents a spherically symmetric, stratified atmosphere. The solid line is temperature and the dotted line is density. (From Vernazza, Avrett, & Loeser (1981)).

The transition region also reflects a change in the morphological structure of the solar atmosphere: images of the sun taken in chromospheric emission lines (e.g. Hα, Ca II and other lines at 5–10,000 K) show a mottled chromospheric network that blurs with increasing height and temperature. This blurring effect is due to the topology of the magnetic network at those heights: at low levels near the photosphere the magnetic concentrations remain tightly bundled but expand to fill the available space with increasing height as the magnetic pressure begins to exceed the gas pressure (Kopp & Kuperus 1968; Feldman, Doschek, & Mariska 1979). Hence, the ability to observe line and continuum emission in the chromospheric and transition regions would provide an additional datapoint in understanding the evolution of emerging magnetic bipoles, which are already well-observed in the photosphere through any number of ground-based solar observatories and also in the corona from instruments such as the Soft X-ray Telescope on *Yohkoh* (Tsuneta et al. 1991).

Skylab and UV images from sounding rocket flights of the chromosphere and transition region show a clear correspondence to the structure of the photospheric magnetic field. The next phase of understanding the solar transition region is a better understanding of the geometry of this region. It has been argued that only a fraction of the transition region connects to the hotter corona, and it has been speculated that much of this region lies in small, closed loops that do not rise to coronal heights. (c.f. Dowdy, Rabin, & Moore 1986 and Mariska 1992; also see figure 2.12 in section 2.7). This observation puts constraints on the pathways providing heat to the transition region, as heat tranfer from the corona preferentially occurs along magnetic lines of force. This implies that closed loop structures in the transition region require some alternative heating mechanism.

The TRACE mission is the next step in this process of understanding the solar chromosphere, transition region and corona. TRACE is a 30 cm aperture Cassegrain telescope with four channels to image solar plasmas in three extra-ultraviolet (EUV) wavelengths and a number of UV wavelengths, covering a spectrum of emission lines over a temperature range from 10,000K–1MK. TRACE will collect images with a spatial resolution of 1.0 arcsec (0.5 arcsec pixels) at a maximum temporal resolution of $\approx$ 5 sec. TRACE was launched April 1, 1998 into a sun-synchronous polar orbit, allowing for continuous uninterrupted observing for eight months, followed by a three month eclipse season, then a second observing period of nominally three months. The baseline mission is for one year.

Chapter 2 of this thesis is a description of the UV channel of TRACE. A brief introduction to the capabilities of the instrument and optics is presented. The TRACE instrument is able to image solar plasmas in the H I Lyα λ1216 Å line, the C IV resonance doublet at 1548 and 1550 Å, the UV continuum centered at 1600 Å and a wide-band white-light image centered at 5000 Å. The method for reducing the UV data to produce photometrically accurate C IV images is discussed in some detail. The C IV resonance doublet is superimposed on a UV continuum that increases six orders of magnitude over 1000 Å, making it quite difficult to observe the C IV emission lines with current multilayer technology. Chapter 2 addresses this problem and suggests a method to filter out the contaminating emission from nearby lines and the underlying UV continuum. The capability to make time-lapse observations of the

C IV emission line pair has not been possible since the *Ultraviolet Spectrometer and Polarimeter* (UVSP, Tandberg-Hanssen et al. 1981) on the *Solar Maximum Mission* (SMM). TRACE will provide higher spatial and temporal resolution over a larger field of view. The combination of high spatial resolution and time-lapse imaging makes TRACE a very provocative mission.

1.2 The Magnetic Field: Connecting the Photosphere and Corona.

Several studies of the evolution of the photospheric magnetic field in quiet sun regions have shown the magnetic structures to be evolving on very rapid timeframes: for magnetic features with fluxes exceeding $\approx 2 \times 10^{18}$ Mx as much flux is cancelled as is present in the quiet-Sun network with in 1.5 to 3 days (Schrijver et al. 1997). Hagenaar, Schrijver, & Title (1997) studied the cellular pattern of the supergranular network from Ca II K filtergrams and found supergranule cell diameters of $L =$ 13–18 Mm. Surprisingly, there is little to be found in the literature discussing the corresponding size and timescales of coronal brightenings in the quiet sun to compare to these findings. Numerous references exist that describe active regions that appear to live for multiple solar rotations, and there are similarly numerous references describing time and length scales associated with X-ray Bright Points (XBPs) (Golub, Krieger, & Vaiana 1976a; Golub, Krieger, & Vaiana 1976b; Strong et al. 1992; Harvey-Angle 1993; Harvey 1997), but a systemmatic comparison of evolution in both the photospheric magnetic field and the quiet solar corona does not appear to exist. In chapter 3 the response of the corona visible in the Fe XII 195Å emission line is compared to the evolution of the underlying photospheric magnetic field and also to the results discussed above. It is found that the quiet corona evolves on timescales of 10–15 hours, in favorable comparison to the lifetime of features in the photospheric magnetic field, and it is also found that small-scale coronal brightenings on average are 18–26 Mm in size, slightly larger than the size of a typical supergranule. Emerging flux tends to evolve and grow continuously on a discontinuous basis: the largest-scale structures in the quiet corona are the product of merging and growing flux concentrations in the photosphere, resulting in coronal reconnection to correspondingly larger opposite polarity concentrations. This amounts to a continuous process of small-scale reconnection in the corona, giving rise to an isotropic distribution of coronal brightenings interacting with opposite polarities from nearest-neighbors to stronger concentrations at significantly larger distances.

CHAPTER 2

UV OBSERVATIONS WITH TRACE

2.1 Abstract

The *Transition Region and Coronal Explorer* is a space-borne solar telescope featuring high spatial and temporal resolution. TRACE images emission from solar plasmas in three extreme-ultraviolet (EUV) wavelengths and several ultraviolet (UV) wavelengths, covering selected ion temperatures from 6000 K to 1 MK. The TRACE UV channel employs special optics to collect high resolution solar images of the H I Lyα line at 1216 Å, the C IV resonance doublet at 1548 and 1550 Å, the UV continuum near 1550 Å and also a white light image covering the spectrum from 2000–8000 Å.

We present an analytical technique for creating photometrically accurate images of the C IV resonance lines from the data products collected by the TRACE UV channel. We use solar spectra from several space-borne instruments to represent a variety of solar conditions ranging from quiet sun to active regions to derive a method, using a linear combination of filtered UV images, to generate an image of solar C IV 1550 Å emission. Systematic and statistical error estimates are also presented. This

work indicates that C IV measurements will be reliable for intensities greater than 10^{14} photons $s^{-1}cm^{-2}sr^{-1}$. This suggests that C IV 1550 Å images will be feasible with statistical error below 20% in the magnetic network, bright points, active regions, flares and other features bright in C IV. Below this intensity the derived image is dominated by systematic error and read noise from the CCD.

2.2 Introduction

The UV spectrum provides a wealth of diagnostics for plasmas in the solar transition region and chromosphere. H I Lyα λ 1216 Å and the C IV resonance doublet at λ 1548 and 1550 Å (hereafter shortened to C IV) in particular are interesting lines for observing plasmas with temperatures from 10–100,000 K. Lyα also provides stunning prominence images at the solar limb. Essentially all transition region models (see Fontenla et al. (1990) and references therein) have Lyα as the main energy loss mechanism below 10^5 K. C IV is an interesting diagnostic in a variety of ways. It has also been suggested (Bruner & McWhirter 1988; Doyle 1996) that the total radiated power of an emitting plasma may be deduced from the intensity of C IV. Hawley & Fisher (1994) suggest that the C IV fluxes serve as a pressure diagnostic under appropriate conditions. Brekke et al. (1996) have observed C IV flare intensities to vary by a factor of $\sim$ 15,000 over pre-flare levels.

However, C IV is a difficult line to observe. At 1550 Å, C IV sits atop a UV continuum background that raises five orders of magnitude in intensity over 1200–3500 Å. Various methods have been attempted to generate a "clean" C IV image. The *Ultraviolet Spectrometer and Polarimeter* on the *Solar Maximum Mission* collected images by rastering a grating over a 256×256 pixel image with 3 arcsecond pixels (Woodgate *et al.* 1980). The spectrometer produced relatively clean images with a temporal resolution of about 3 minutes. The *High Resolution Telescope and Spectrograph* (HRTS) sounding rocket experiment employed a tandem Wadsworth Spectrograph with spatial resolution of 1 arcsecond along a 1000 arcsecond slit. HRTS was able to step the slit to cover a 10×800 arcsecond region in 20 seconds. Consequently HRTS was able to map a portion of the solar atmosphere as a function of time (Dere et al. 1984). HRTS used a spectrograph to establish spectral purity. The *Solar Ultraviolet Measurements of Emitted Radiation* (SUMER) experiment on the *Solar and Heliospheric Observatory* is a spectrograph capable of stepping across the solar disk to generate full-sun images with pixel sizes of ~ 1 arcsec px^{-1} and 20-40 mÅ px^{-1}, again at the expense of temporal resolution (Wilhelm et al. 1995). The *Solar Physics Plasma Diagnostics* (SPDE) rocket payload (Damè et al. 1996) observed in C IV and neighboring wavelengths using multilayer optics in the *Transition Region Camera.* The design approach for this instrument was the catalyst for the TRACE UV channel.

The UV channel of TRACE has been designed from the beginning with the intent of estimating C IV emission on a strong UV background. The UV filters in TRACE were chosen to satisfy this requirement, and an analysis with sample solar spectra has been performed to illustrate this approach.

2.3 The TRACE Instrument

2.3.1 Overall Description

The TRACE instrument is a 30 cm aperture Cassegrain telescope intended to observe solar plasmas from 6000 to 1 MK with 1 arcsecond spatial resolution and with high temporal resolution and continuity (Tarbell et al. 1994). The optical path of the

Table 2.1: Telescope Characteristics.

Primary Mirror Diameter	30 cm
Effective Focal Length	8.66 m
Pixel Size	21 × 21 μm
	0.5 × 0.5 arcsec
CCD Size	1024 × 1024 pixels
Field of View	8.5 × 8.5 arcmin
Wavelength Channels:	Fe IX λ171 Å
	Fe XII λ195 Å
	Fe XV λ284 Å
	H I Lyα λ1216 Å
	C IV λ1550 Å
	White Light λ5000 Å
Image Stabilization	± 0.1 arcsec

telescope is illustrated in figure 2.2 and the principal characteristics are given in Table 2.1.

To provide wavelength discrimination the telescope is divided into four quadrants, each of which is sensitive to a different wavelength range. Three of these quadrants are sensitive in the extreme ultraviolet (EUV) and the fourth in the far UV through the visible wavelengths. The EUV quadrant bandpass selections are determined by multilayer coatings on the primary and secondary mirrors. The UV quadrant employs a narrowband all-dielectric primary mirror coated for wavelength selection and a MgF_2/Al overcoated secondary mirror. Further wavelength discrimination is accomplished via a selection of broadband and narrowband filters. Visible light is excluded from the EUV quadrants by thin aluminum entrance filters mounted on a nickel mesh in front of each EUV quadrant. The UV quadrant is shielded by a broadband UV filter. A quadrant selector located directly behind the entrance filters selects which of

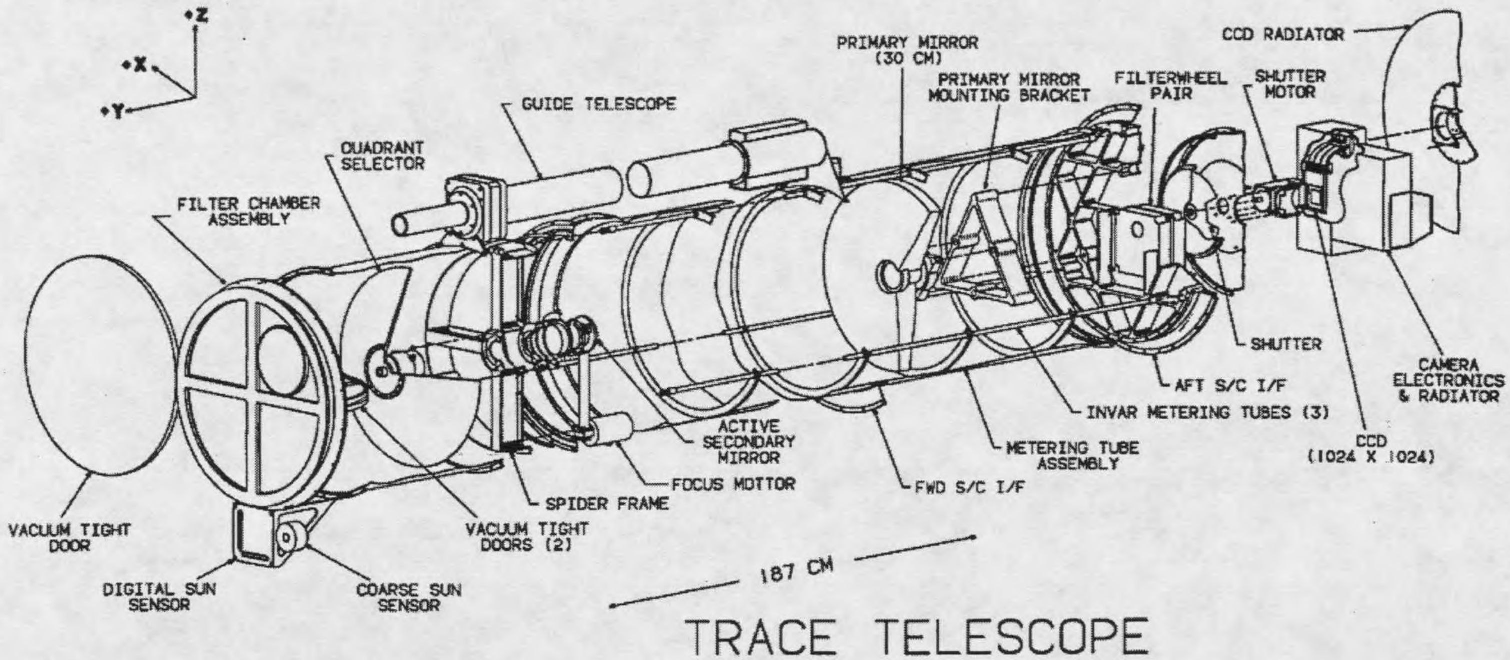

Figure 2.1: The TRACE Instrument.

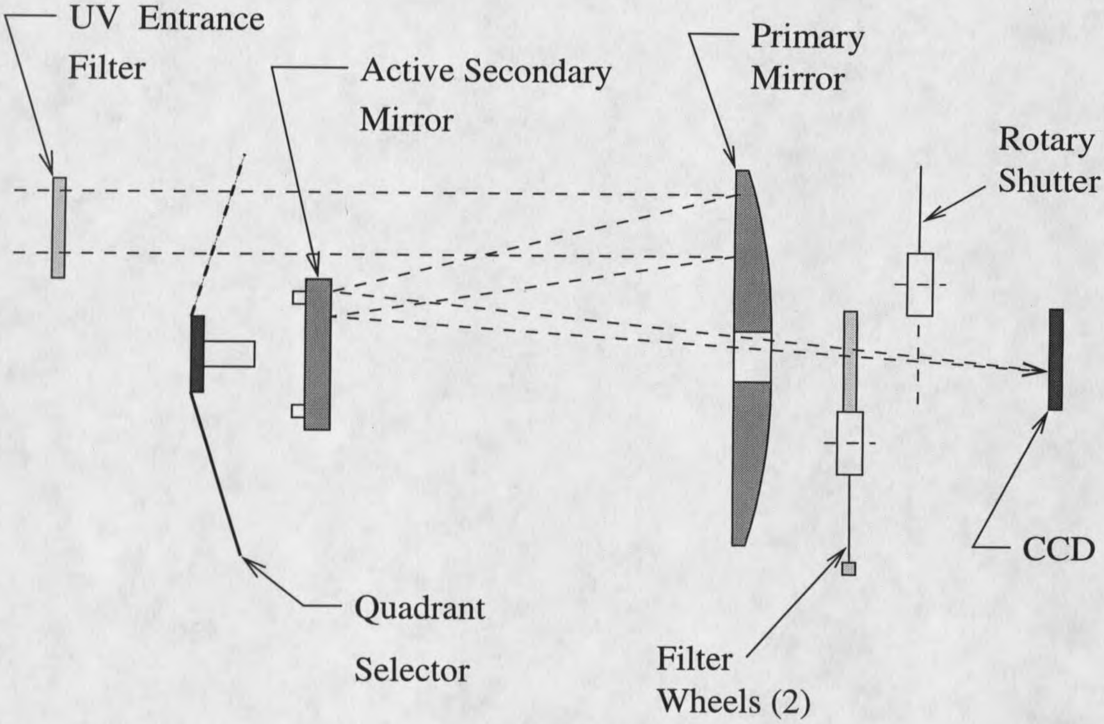

Figure 2.2: The TRACE Optical Path.

the four channels is active. Two filter wheels, located aft of the primary mirror, provide further stray light rejection in the EUV and wavelength selection at the various UV wavelengths. The filtered images are detected by a lumigen-coated[1] CCD.

CCD images are collected by the data handling computer (DHC) which buffers full-frame or partial-frame data from the CCD into the DHC main memory. The control computer (CC) establishes the quadrant selector position, focus, filter wheel position and exposure time. In addition, the CC specifies the data compression and scientific data processing to be performed by the DHC. Data from the DHC is then transferred into the spacecraft mass memory where it is stored until downlink. The DHC functions have an execution speed consistent with an observing cadence of one

[1]Substantial confusion exists on the spelling of "lumigen". It is referred to in the literature as lumigen, liumogen and lumogen. All refer to the same material.

full CCD image every 5 seconds; smaller extracted sub-images can be taken at a cadence of one per second.

2.3.2 TRACE UV Channel Description

The UV channel of TRACE posed a restrictive set of requirements on the optics. One design goal was to be able to image both Lyα and C IV emission. A subsidiary goal was to acquire a useful image in the visible continuum at an exposure greater than $\approx$ 20 ms. Imaging at Lyα and C IV imposed the most difficulty on the design because this mandated a need for a broadband filter in the UV that would provide adequate transmission at both of the UV wavelengths while providing sufficient rejection at the longer wavelengths. It was necessary to balance transmission, rejection and bandpass to optimize 1216 Å and 1550 Å throughput. All UV coatings were designed and manufactured by Acton Research Corporation (Acton, MA).

The entrance window is a single crystal 118 mm dia.$\times$10 mm thick MgF_2 substrate coated with a broadband multilayer metal-dielectric interference coating. The coating was optimized to transmit about equally at 1216 Å and 1550 Å while simultaneously providing good rejection at the visible wavelengths.

The primary and secondary mirror coatings are a compromise between reflecting Lyα and C IV and rejection of visible light (wavelengths out of the bandpass are transmitted into the mirror substrate; the coating is nearly transparent to the human eye). The primary mirror is coated with an all-dielectric multilayer interference coating with peak reflection of approximately 83% at 1540 Å and a bandwidth of 150

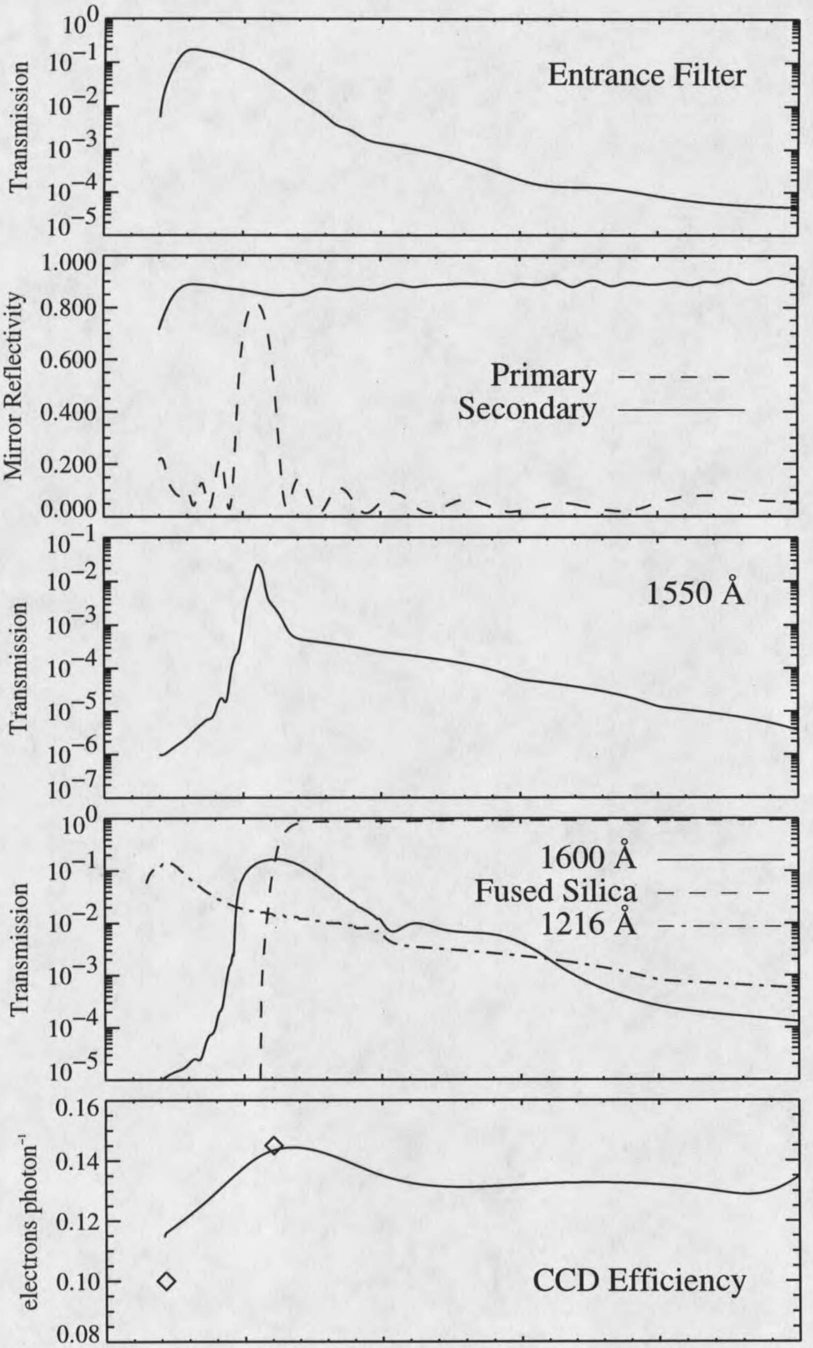

Figure 2.3: UV response of the individual UV optical components of TRACE. The data points in the bottom graph at 1215 and 1605 Å show measured efficiency of witness samples Lumigen-coated with the TRACE CCD. See text.

Table 2.2: TRACE Filter Properties

Solar Emission	Substrate	Central Wavelength	FWHM	Peak Transmission
Carbon IV	CaF_2	1550 Å	37 Å	2.4%
H I Lyman α	MgF_2	1216 Å	80 Å	14.1%
UV Continuum	Crystalline Quartz	1600 Å	245 Å	16.6%
White Light	Fused Silica	N/A	N/A	94%

Å FWHM. The reflectivity drops to 10% at 1216 Å and wavelengths above 1600 Å. The primary is designed to enhance the signal-to-noise ratio for C IV by rejecting long-wavelength contamination. This coating has the side effect of reducing the heat load and UV flux on the secondary mirror. The UV quadrant of the secondary mirror is coated with aluminum and a thin film MgF_2 overcoating to prevent oxidation and optimize the coating for 1550 Å.

The filter wheels contain the UV filters described in table 2.2 and figure 2.4. The filters of interest for this problem are the 1550 Å filter, the 1600 Å filter and the Fused Silica filter. In figure 2.3 we show the transmission curves for these filters. The 1550 Å filter is particularly noteworthy as it is a induced transmission filter (Macleod 1986). Extra-narrowband filters with this bandpass typically suffer from sidebands which contaminate the desired emission line; the filter used in TRACE does not. This filter has a FWHM of 37 Å and long-wavelength rejection of order 10^{-6}. The 1600 Å filter is a narrowband filter with FWHM of 245 Å and will be used in tandem with the fused silica filter to evaluate the long-wavelength continuum. Substrate thickness for each of the UV filters was specified so as to minimize change in focus when switching between wavelengths.

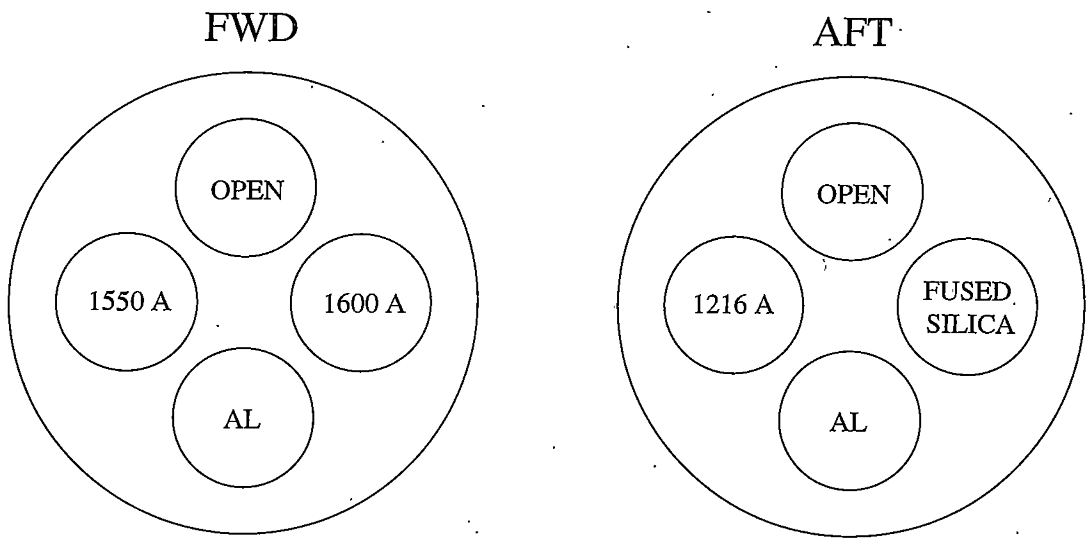

Figure 2.4: Filter layout in forward and aft filter wheels, as viewed from the front of the telescope.

The TRACE CCD (three-phase, multi-pinned phase, unthinned, front-illuminated) is almost identical to the detector used in the Michelson Doppler Imager (MDI, Scherrer *et al.* 1995) on SoHO and is in fact an MDI flight spare made by Loral Aerospace Corporation. The front surface is coated with lumigen. Lumigen is a fluorescent coating that sensitizes the CCD to UV and EUV wavelengths (Deeg & Ninkov 1995; Kristianpoller & Dutton 1964). The quantum efficiency (QE) measurements used in this analysis are taken from the Ford/CRAF Cassini CCD (Janesick 1994, private communication) as the TRACE CCD is similar to that device. The broadband coverage provided by the above measurement makes the analysis in this paper possible. Slides coated with the TRACE CCD have been measured at 1215 Å and 1605 Å (c.f. the bottom curve in figure 2.3). The TRACE CCD is $\approx$ 12% lower in quantum efficiency at Lyα and nominally the same at 1605 Å. The photodiodes used for this calibration have a 10% absolute uncertainty in their quantum efficiency. Since the

1215 Å result has little effect on the C IV analysis, the Cassini measurements were used verbatim for the calculation that follows.

2.4 C IV Analysis

2.4.1 Photometry and Analysis

The optical response of the UV quadrant may be represented by the relation

$$I(\lambda, t) = F(\lambda, t)T(\lambda)Q(\lambda)\Omega A \tag{2.1}$$

where $I(\lambda, t)$ represents the number of electrons pixel^{-1} Å^{-1} s^{-1} generated at the CCD, $F(\lambda, t)$ represents the solar flux with units of photons s^{-1} Å^{-1} cm^{-2} sr^{-1}, $T(\lambda)$ represents the combined optical response of the mirrors and analysis filters, $Q(\lambda)$ represents the quantum efficiency of the detector (electrons photon^{-1}), Ω represents the solid angle subtended by one pixel (0.5×0.5 arcsec or $\approx 5.876 \times 10^{-12}$ sr) and A represents the clear aperture of the UV quadrant (91.0 cm^2). Note that the CCD doesn't actually yield a solar spectrum but yields a detection rate integrated over all wavelengths: $I(t) = \int_\lambda F(\lambda, t)T(\lambda)Q(\lambda)\Omega A d\lambda$.

A complete C IV dataset is composed of three images:

$$\begin{aligned} I_1 &= 1550 \text{ Å Image} \\ I_2 &= 1600 \text{ Å Image} \end{aligned} \tag{2.2}$$

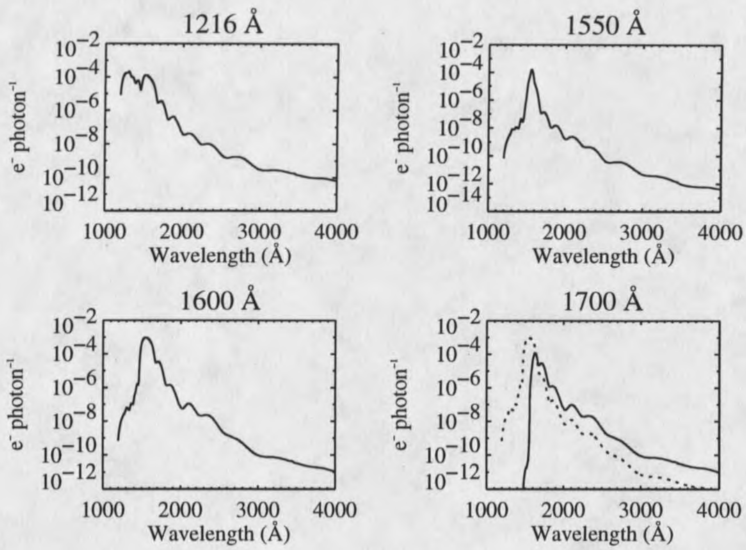

Figure 2.5: Spectral response of the UV channel. The 1700 Å image is composed of an image with the 1600 Å filter in series with a fused silica substrate. The dotted curve in the lower right-hand graph represents a "clean 1600 Å" curve given by the difference between the 1600 Å and scaled 1700 Å images as described in equation 2.4.

$$I_3 = 1700 \text{ Å Image} = 1600 \text{ Å+Fused Silica Filters}$$

The quantity $[T(\lambda)Q(\lambda)\Omega A]$ in equation 2.1 describes the response function of the instrument. This quantity can then be calculated to yield response curves at the various wavelengths of interest. Response function curves for the Lyα channel and images I_1, I_2 and I_3 are given in figure 2.5. The Lyα channel has a double peak at 1216 and 1550 Å. This is a result of the transmission of the Lyα filter coating and the coating on the primary, which is centered at 1550 Å. The 1700 Å image is a product of the 1600 Å filter in series with the fused silica substrate. The purpose of this combination is to measure the contribution from long-wavelength contamination.

Given the above three measurements, it should be possible to estimate three portions of the solar spectrum:

$$\begin{aligned} I_{CIV} &= \text{1550 Å Intensity} \\ I_{CTN} &= \text{Ultraviolet Continuum} \\ I_{WL} &= \text{White-light Continuum} \end{aligned} \tag{2.3}$$

The goal of this exercise is to generate these three quantities from equations (2.2). This is done via a least-squares analysis with sample spectra from the HRTS mission. As a first step, however, it is useful to apply some physical intuition to the problem to eliminate one variable. The latter two images in (2.2) may be combined to generate a single "clean" narrowband UV continuum image near 1550 Å with a FWHM of ≈ 200 Å via the relation:

$$I_{2C} = I_2 - (1.07)I_3. \tag{2.4}$$

Each of the two resulting images (I_1 and I_{2C}) may be resolved into a linear combination of contributions from Lyα and the UV continuum. This method suggests the following relationship:

$$\begin{aligned} I_{CIV} &= \alpha I_1 + \beta I_{2C} + \epsilon_{CIV} \\ I_{CTN} &= \gamma I_1 + \delta I_{2C} + \epsilon_{CTN}, \end{aligned} \tag{2.5}$$

where α, β, δ and γ are constants and ϵ_n represents the systematic error in this measurement. I_{CIV} and I_{CTN} represent the contributions from the C IV and UV continuum emission, respectively.

The TRACE response for a nominal active region spectrum is illustrated in figure 2.6.

2.5 Error Propagation

In the previous section we constructed a set of equations to calculate the intensity in C IV and the UV continuum at 1550 Å. In this section we derive the statistical error in the data due to Poisson counting statistics.

For the three images of equation 2.2, the error due to photon statistics and read noise in the CCD is given by

$$s_n = \sqrt{\frac{I_n}{t_n} + \left(\frac{RN}{t_n}\right)^2} \tag{2.6}$$

In (2.6), I_n represents the intensity of a pixel in each respective image, s_n represents the standard deviation of the corresponding photon detection rate, t_n represents the exposure time and RN is the read noise of the CCD ($\sim$ 20 electrons).

In equation 2.4 we derived a 1600 Å continuum image bereft of visible contamination, and the corresponding error is given by

$$s_{2C} = \sqrt{s_2^2 + (1.07)^2 s_3^2} \tag{2.7}$$

where the factor of 1.07 is the scaling factor due to the fused silica substrate. It then

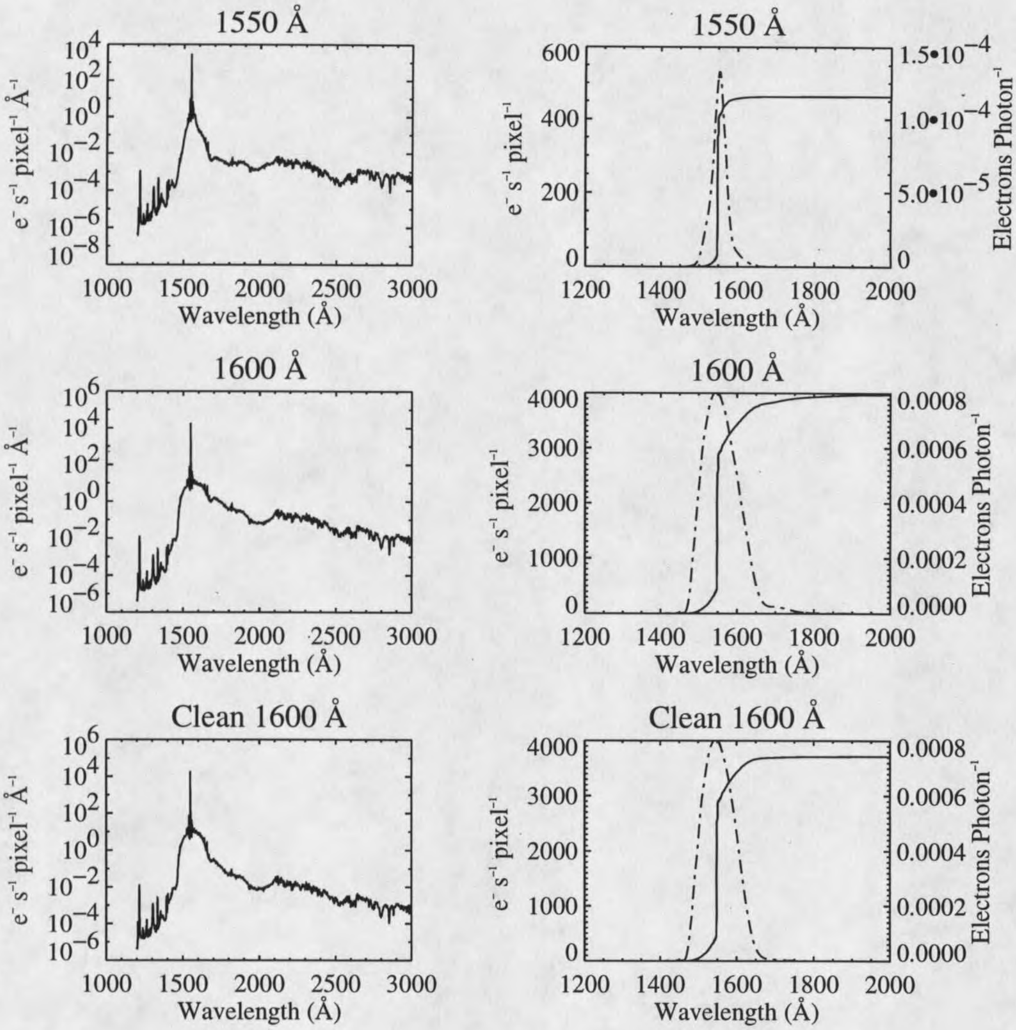

Figure 2.6: TRACE instrument response to an active region solar spectrum. The "Clean 1600 Å" spectra is a difference of the 1600 and scaled 1700 Å spectra. The curves at right indicate (solid line, LHS) the running integral contribution to the CCD signal, and (dotted line, RHS) the instrument throughput.

follows that the uncertainty in the calculated C IV and continuum levels is given by

$$s_{CIV} = \sqrt{\alpha^2 s_1^2 + \beta^2 s_{2C}^2} \quad (2.8)$$
$$s_{CTN} = \sqrt{\gamma^2 s_1^2 + \delta^2 s_{2C}^2}$$

At this point, we've mentioned two forms of error: the systematic error in the calculation contained in ϵ, which is the absolute error in the calculation for a given solar spectrum, and the error due to photon statistics contained in s_n. In the Error Analysis section we present results of both types of error for the dataset used in this paper, calculated as a fractional error – the ratio of the error to the desired answer. In this guise, a fractional error of 1.0 indicates the uncertainty is equal to the desired answer. It is possible that the systematic error may be improved upon through new techniques and on-orbit calibrations, but the standard deviation is unlikely to change significantly. Improvements to the standard deviation will only be seen in significantly longer exposure times or brighter sun.

2.6 C IV Estimates

2.6.1 Spectral Data

To predict the results for TRACE we compiled a set of solar spectra to fold through the optical response function. UV data are only available from spaceborne instruments, and no single instrument has been able to collect data over the large spectral range

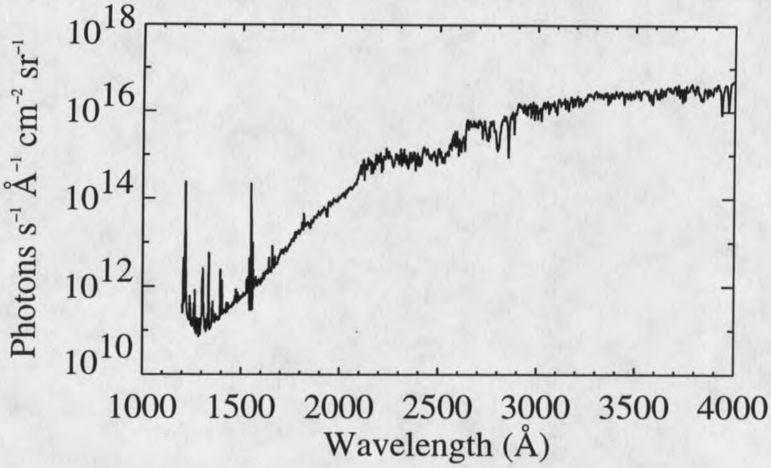

Figure 2.7: Representative network solar spectrum from SOLSTICE and HRTS.

we are interested in: ~1200–10000 Å. It was therefore necessary to obtain data from several sources and merge the spectra together (see figure 2.7).

The SOLSTICE instrument (Rottman, Woods, & Sparn 1993) is a rich source of irradiance spectra but is limited in that the spectral resolution is only 1.5 Å and it provides only a full-disk average intensity. This dataset provided a useful spectral baseline and covered the spectral range 1200–4000 Å. To provide for better spectral resolution and to also reflect solar variability from quiet sun to active regions, we employed HRTS data over the 1540–1559 Å range (Brekke 1993; Brekke & Kjeldseth-Moe 1994). To fill out the visible and infrared spectrum to the upper limit of the CCD response (1 μm) we employed radiance spectra from Pierce & Allen (1977). We are combining radiance (a measurement of the intensity at the source) and irradiance (the intensity as measured at 1 AU) data in this model. While this is not a completely accurate method of creating a sample solar spectrum, it is sufficient for our purposes.

The solar spectrum is accurate within the bandpass of the instrument (1400-1800 Å), and the approximated spectrum above and below this region only provides a minor contribution to the image.

The HRTS data (P. Brekke 1995, private communication) provide a comprehensive set of stigmatic spectra over the range 1540–1559 Å across a large extent of the solar disk from near sun center to the solar limb. Each spectral trace in this dataset was in turn matched to the SOLSTICE data. For $\lambda < 1540$ Å SOLSTICE was scaled by a constant to match continuum levels of the HRTS data. For 1559 Å $< \lambda <$ 2100 Å, the SOLSTICE spectra was scaled by a function matching the continuum at 1559 Å. The scaling function was constrained to be unity at 2100 Å, where the variability of the solar disk is lower and the throughput of the TRACE instrument is down by several orders of magnitude.

2.6.2 Results

In order to solve for the coefficients in eqn. 2.5 it is necessary to define *a priori* what I_{CIV} and I_{CTN} represent. For this study I_{CIV} represents the emission from the C IV doublet at 1548 and 1550 Å with the UV background removed, and I_{CTN} represents the UV continuum and other emission lines in the range 1540–1559 Å. The continuum definition is somewhat arbitrary but represents the UV filters in TRACE reasonably well. The UV response of the system was then convolved with the merged HRTS/SOLSTICE spectra to predict the TRACE response to a variety of solar C IV and UV continuum emission features. We then calculated the actual emission, compared it to the observed intensities in each of the filter combinations and generated the set of solutions to equations 2.5 via a least-squares analysis:

$$\begin{pmatrix} \alpha & \beta \\ \gamma & \delta \end{pmatrix} = \begin{pmatrix} 2.69 \times 10^{13} & -1.96 \times 10^{12} \\ -5.86 \times 10^{12} & 9.31 \times 10^{11} \end{pmatrix}. \qquad (2.9)$$

Given the above coefficients, it is possible to make empirical estimates of the measurement errors. The following calculations were generated with exposure times of 10 seconds for 1550 Å, 2 seconds for 1600 Å and 5 seconds for 1700 Å. There are two sources of error to consider. The first and easier to quantify is that due to Poisson statistics and read noise in the TRACE CCD, illustrated in figure 2.8. Below a C IV intensity of $\sim 10^{14}$ photons $s^{-1}cm^{-2}sr^{-1}$ the signal is dominated by the read noise of the CCD and will be manifested in the images by noise in the image and other spurious artifacts. This threshold intensity suggests we will be able to calculate useful numbers for bright network, active regions, flares and other relatively bright features. Somewhat fainter features will be measureable only with significantly longer exposure times.

We are also able to examine the systematic error that is a result of this method of calculation; this is reflected in the term $\epsilon_{\rm CIV}$ in equation 2.5. We calculate this term by folding the HRTS dataset through equation 2.5 given the derived values in equation 2.9, and then comparing the calculated I_{CIV} to the actual line intensity. These results are presented in figure 2.9. They do not quite reflect reality as the variability of the emission lines outside 1540–1559 Å contaminating the C IV image was not considered

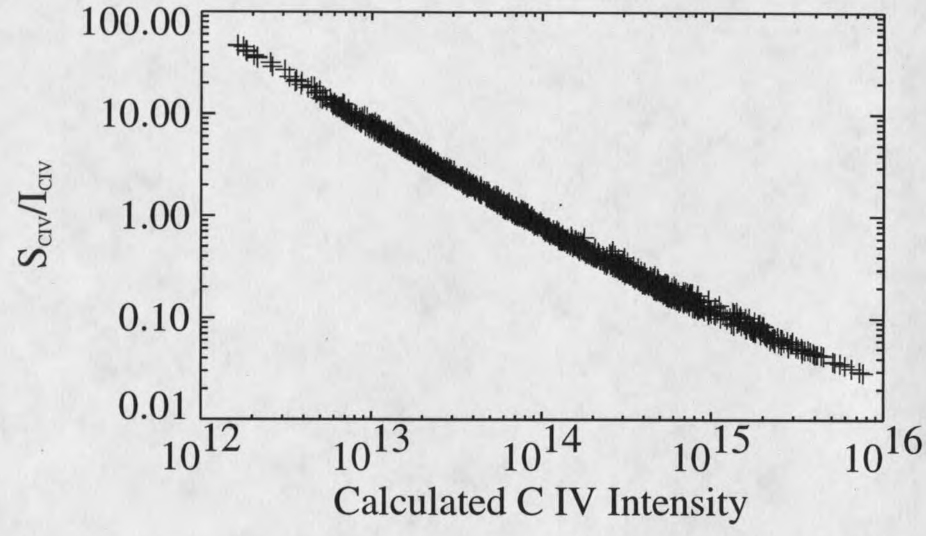

Figure 2.8: Fractional standard deviation of the calculated C IV intensity based on Poisson counting statistics and a CCD read noise of 20 e^{-}. Below an intensity of $\sim 10^{14}$ photons $s^{-1}cm^{-2}sr^{-1}\text{Å}^{-1}$ the noise is dominated by CCD read noise. Standard deviation is based upon a 10 second 1550 Å exposure, a 2 second 1600 Å exposure and a 5 second 1600 Å+fused silica exposure.

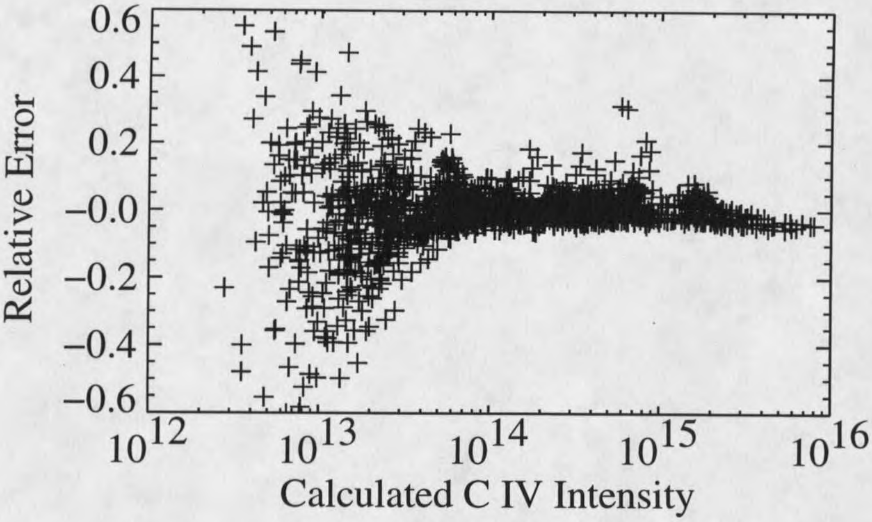

Figure 2.9: Relative systematic error (ϵ_{CIV}/I_{CIV}) observed in calculating C IV intensity from the HRTS data. Intensity is in units of photons $s^{-1}cm^{-2}sr^{-1}$.

in this exercise. The narrow bandwidth of the filters however should serve to minimize this effect. Based on these results we can expect a systematic error of less than 20% for bright features.

It is interesting to generate a linear combination of the 1550 Å, 1600 Å and 1700 Å filters as suggested by equations 2.5. This results in a set of "effective filters" for C IV and the UV continuum emission illustrated in figure 2.10. The graphs are a pleasing visual check of the C IV and continuum extraction techniques. The C IV "filter" is heavily weighted towards the C IV emission line, while the resulting UV continuum "filter" attempts to isolate the continuum around 1550 Å while rejecting C IV. The negative transmission present in the C IV curve is in effect a method of measuring the mean intensity for the underlying UV continuum at 1550 Å.

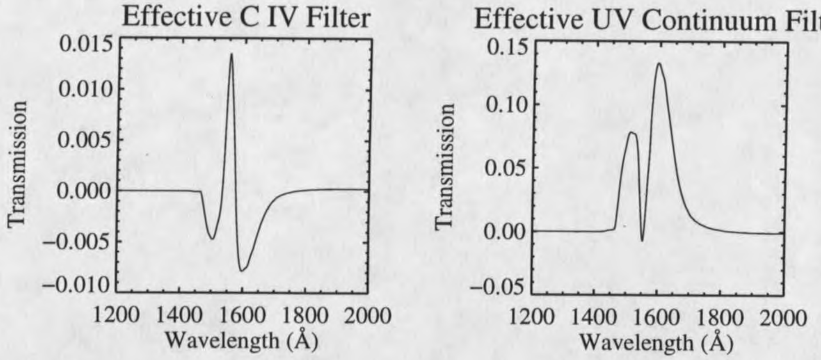

Figure 2.10: Effective Transmission of the TRACE C IV and UV continuum channels. These curves represent a linear combination of the 1550 Å, 1600 Å and 1700 Å response functions. The effective C IV filter isolates the 1550 Å lines, while the continuum filter rejects these lines.

2.7 Results from Post-Launch

The TRACE instrument launched on April 1, 1998. After an initial outgassing, calibration and commissioning phase dedicated science observing began in earnest on April 20, 1998. The triad of images included here (see figure 2.11) were taken during the initial 30-day plan at 29-APR-98 11:43:00UT.

The raw images are shown in figure 2.11 and the reduced images are shown in figure 2.12. The average count rates in all images are detailed in table 2.3. It is evident that the count rate in all channels is higher than anticipated; this has also been noted in White Light exposures (C. J. Wolfson 1998, private communication). This is likely due to a higher transmission through the UV entrance filter at wavelengths greater than $\sim$ 2100 Å, as the increase in long wavelength signal is consistent in all three filtergrams and is most noticeable in the 1700 Å filtergram which is predominantly these long wavelengths. Further analysis and cross-correlation with other instruments

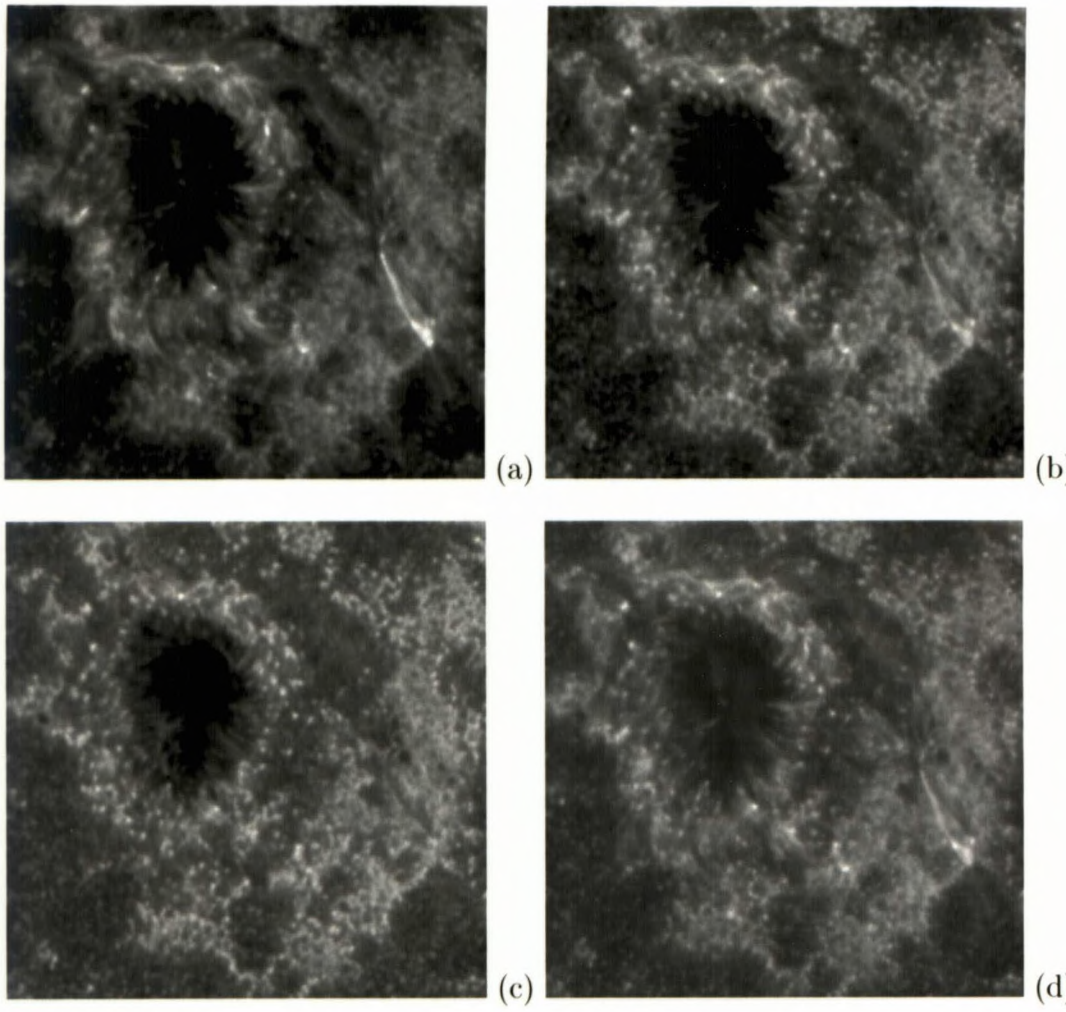

Figure 2.11: UV Filtergrams from TRACE. (a) is the narrowband (30 Å FWHM) 1550 Å C IV image, (b) is the broader (275 Å FWHM) 1600 Å UV continuum image, (c) is the long wavelength 1700 Å image and (d) is the I_{2C} image as detailed in equation 2.4. This set of images was taken at 29-APR-98 11:43:00UT. North is up and East is to the left. The images are 256 × 256 pixels and the pixel size is 0.5 arcseconds. The exposure time for the three images above were 8.2 seconds, 1.0 seconds and 2.0 seconds respectively.

will be required to better quantify this long wavelength leak.

Table 2.3: TRACE Image count rates comparisons.

Image	Predicted Count Rate ($e^{-}s^{-1}pix^{-1}$)	Observed Count Rate ($e^{-}s^{-1}pix^{-1}$)
1550 Å	460	550
1600 Å	4000	7600
1700 Å	300	2600
Clean 1600	3700	4800

The derived C IV images, however, are very interesting and are shown in figure 2.12. Filamentary structures around the sunspot are visible and small, relatively cool C IV loops are visible at various locations in the image. The continuum image does not show these loop structures and is rather difficult to interpret. The intensity distribution in the C IV image is well above 10^{14} photons s^{-1} cm^{-2} sr^{-1}, sufficiently strong as to have a small relative error in the bright loop structures (c.f. § 2.6.2, in particular figures 2.8 and 2.9). The structures in the dark sunspot are likely an artifact of the analysis procedure.

In light of the new results from the TRACE instrument there are inevitably changes to be made in the observing sequences. Early movies from TRACE show features that vary in intensity and evolve on timescales faster than the TRACE instrument can resolve, on the order of 5–10 seconds. Early plans suggested taking a set of 1600 and 1700 Å images and then rapidly generating 1550 Å filtergrams, then using the first images to do the C IV derivation. The rapid evolution of the transition region is frustrating these efforts, however, and it is likely that other methods of C IV analysis will prevail. Current efforts lean towards estimating the C IV emission from only a pair of filters: the 1600 and 1700 Å filters, for example, may be used to generate high-speed movies with a cadence of just a few seconds. In active regions this should be sufficient to get a gross estimate on the C IV emission at a higher cadence at the expense of photometic accuracy.

2.8 Discussion

We have presented a method of estimating C IV 1550 Å emission from the UV dataset that will be collected by the TRACE instrument. Data from the SOLSTICE and HRTS missions were combined with ground-based data to generate a large set of synthetic solar spectra to model TRACE performance. Coefficients were generated via a least-squares fit to generate a set of linear equations for estimating the true C IV and UV continuum levels from the TRACE UV dataset. The data were then folded back through this system to generate Poisson statistics and an analysis of the systematic (e.g. relative) error in this system. Our analysis suggests that the best results will be achieved in regions of C IV λ 1550 Å intensity greater than $\approx 10^{14}$ photons $s^{-1}cm^{-2}sr^{-1}$. Below this intensity the calculation becomes overwhelmed by CCD read noise, counting statistics and the simplistic nature of the model used in this analysis. It is possible to imagine a more advanced model that varies with intensity and solar conditions, but this quickly becomes both difficult and error-prone

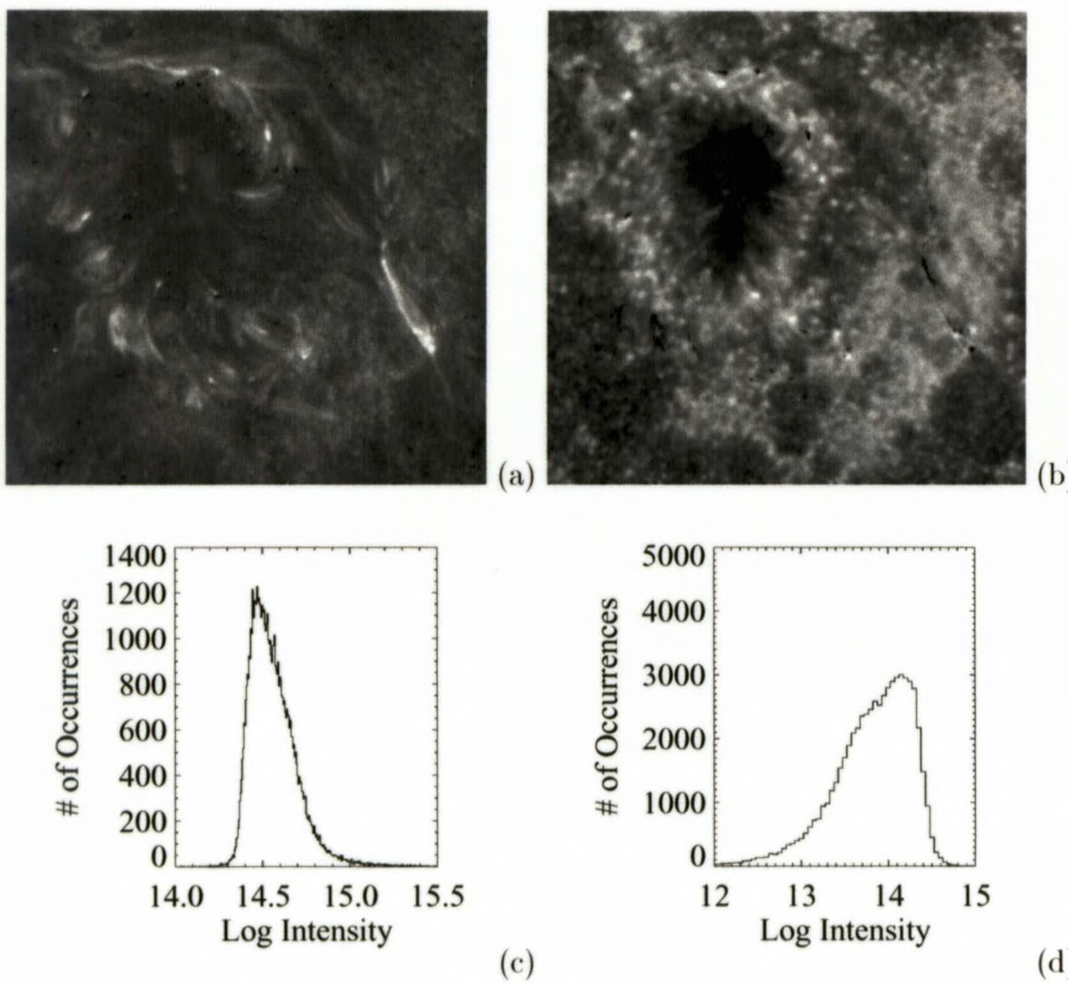

Figure 2.12: Images (a) and (b) are the derived C IV and UV continuum intensities respectively found per equations 2.5 and 2.9. The field of view is 256 × 256 0.5 arcsecond pixels; North is up and East is to the left. Figures (c) and (d) are the intensity distributions in (a) and (b), respectively.

notion. For each pixel, there are only three measurements available from the different filter combinations. This small quantity of information is not sufficient to support a dramatically more complex algorithm.

The manner in which the UV channel has been designed allows for some flexibility in formulating observing sequences. The Lyα channel will be of particular interest near the beginning of the mission, as it will provide an opportunity to observe this wavelength with high temporal cadence for an extended period of time. It will be important to utilize this capability early in the mission, as it should be assumed there will be degradation in Lyα response due to contamination and radiation damage to the lumigen coating on the CCD. To aquire C IV 1550 Å data, the method as suggested in this paper is to always collect a triplet of exposures in 1550, 1600 and 1700 Å. A typical cadence for such an exposure set would be on the order of 30 seconds.

There is some evidence that suggests the brightest features in the C IV lines will also be evolving the most rapidly, and thus critical data in the evolution of these features may pass unobserved. There are several ways of approaching this problem. One method would be to only collect occasional images in the UV continuum at 1600 Å and 1700 Å and then a rapid sequence of 1550 Å images, using the first pair of background images to correct each frame for C IV emission. Another technique that may be considered is to merely take a rapid sequence of images through the 1600 Å filter. This image will contain a large UV continuum background component, but the brightest and most rapidly varying features will likely be emitting in the C IV resonance lines. This may provide a technique to see C IV "blinkers".

Lastly, the fused silica filter will be used to generate short exposure ($\approx$ 20 msec) white light images with a cadence of a few seconds. These images will contain almost equal contributions over the spectral range 2000–8000 Å.

With added experience and on-orbit calibration, refinements to the model presented here is expected. It is anticipated that the SUMER experiment will be able to participate in limited coordinated observations during the early TRACE mission. It is also possible that some coordinated calibration work may be done with various full-sun UV irradiance experiments, e.g. SOLSTICE and the Solar Ultraviolet Spectral Irradiance Monitor (Lean et al. 1992).

CHAPTER 3

MAGNETIC CONNECTIONS IN THE QUIET CORONA

3.1 Introduction.

The mechanisms responsible for heating the solar corona to temperatures in excess of 1 MK have puzzled researchers since the initial discovery of the highly ionized elements in the corona almost 60 years ago (Edlén 1937; Grotrian 1939). Extreme Ultraviolet (EUV) and X-ray solar observations became possible with the advent of the space program. Since the first observations of the sun in X-rays (Blake et al. 1963) there have been many missions of varying complexity and duration ranging from suborbital rocket flights observing for only a few minutes at a time to missions running continuously for years. Perhaps some of the most well-known observatories (but by no means all) would include the S-054 X-ray telescope on *Skylab* (Vaiana et al. 1977), the X-ray Polychromator (Acton et al. 1980) and the Ultraviolet Spectrometer and Polarimeter (Woodgate et al. 1980) on the *Solar Maximum Mission*, the Soft X-ray Telescope on *Yohkoh* (Tsuneta et al. 1991), the Extreme ultraviolet Imaging Telescope on the *Solar & Heleiospheric Observatory* (Delaboudinière et al. 1995) and most recently the *Transition Region and Coronal Explorer* (TRACE, Title et al. 1995, also see § 2). The quality of these observations have improved dramatically through numerous technological improvements which have in turn yielded improved spatial and temporal resolution, improved coverage over longer time intervals and the ability to observe many aspects of the solar atmosphere nearly simultaneously. These improvements in capability have made it possible to study increasingly smaller structures ($\sim$ 1 arcsec or 725 km in EUV and X-rays) and more rapidly evolving phenomena (with cadences on the order of $\lesssim$ 10 sec). However, although we can observe the sun in finer detail than ever before, even the most basic mechanisms driving physical processes on the sun — the methods of heating the corona and the role of the magnetic field in this process, for example — continue to elude us.

In this chapter we present an analysis of a sequence of joint EIT Fe XII (λ 195 Å) observations of the $\sim$ 1.6 MK solar corona and MDI longitudinal photospheric magnetograms of the quiet sun near disk center. For a period of 85 hours MDI obtained one magnetgram per minute its high-resolution field of view and EIT concurrently imaged the solar corona at a cadence of $\approx$ 16 minutes for the duration of the campaign (§ 3.2.2). This campaign provided an unprecedented opportunity to observe the evolution of the photospheric magnetic field and the solar corona at a high temporal cadence for such a long period of time.

We take this opportunity to consider the evolution of the quiet solar corona in response to the activity of the photospheric magnetic field over the duration of the campaign. An understanding of the physical relationship between the evolution of the underlying photospheric magnetic field and structures in the corona is one requirement for understanding the processes responsible for driving the resultant formation and evolution of coronal brightenings. We describe the qualitative evolution of the corona in response to the motions of the photospheric flux concentrations, we look for corresponding length scales in the photospheric magnetic field and the solar corona, and we compare our observations to theoretical predictions of flaring and heating mechanisms in quiet sun coronal loops.

3.1.1 Length and Time Scales of Coronal Structures.

Numerous studies have shown that coronal brightenings correlate very strongly with the locations of magnetic bipoles in the photosphere and chromosphere (Golub et al. 1977; Kankelborg et al. 1996; Falconer et al. 1997; Schrijver et al. 1998). The first measurement of a supergranular length scale in the photosphere is that of Simon & Leighton (1964), who autocorrelated photospheric dopplergrams to find typical length scales of $\approx$ 32 Mm. Since then, extensive studies using autocorrelation (AC) methods and manual measurements of dopplergrams and Ca II K spectroheliograms have yielded characteristic cell sizes on the order of $\approx$ 25–32 Mm (c.f. Hagenaar, Schrijver, & Title (1997) and references therein). Hagenaar, Schrijver, & Title 1997 used a "basin-finding" algorithm to outline cells in Ca II K filtergrams and found a significantly smaller cell size of typically 13–18 Mm. They argued that the difference in cell sizes is a result of the AC method preferentially selecting larger cells. The result of this effect is that the AC method measures a cell area that lies between the second and third moments of the size distribution function, rather than the desired first moment.

Observers have assigned rather arbitrary sizes to the class of objects known as X-ray Bright Points (XBPs) or more generally coronal bright points, typically on the order of $\lesssim$ 20-60 arcsec (Golub et al. 1974; Golub, Krieger, & Vaiana 1976a; Golub 1980; Webb et al. 1993). Golub, Krieger, & Vaiana (1976b) determined the lower bound of their bright point observations was dictated by instrument resolution. Kankelborg et al. (1996) analyzed a selection of bright points from Fe XII (195 Å) and Si XII (44 Å) observations which had a typical size of 3.5–11.5 Mm. Images from the most recent EUV/X-ray instruments (EIT on SoHO, the SXT on *Yohkoh*) routinely show coronal brightenings at the limit of instrumental resolution, $\lesssim$ 3.8 Mm. The recently launched TRACE instrument shows brightenings at its instrumental resolution of 1 arcsec (Schrijver, 1998, private communication).

It stands to reason that there should be a length scale common to both the separation of flux concentrations in the photospheric magnetic field and the size of bright structures in the corona. Observations suggest that relatively bright emerging loops in quiet sun regions never get longer than typically 14 Mm before reconnecting to other neighboring flux concentrations (§ 3.4). This curious result would seem to imply a similar scale size should be present in the photospheric magnetic field. Finding these comparable scale sizes is difficult: the first cut at using nearest-neighbor distances to calculate a scale size doesn't account for the simple fact that coronal loops aren't necessarily bound to their nearest neighbor.

It is also interesting and complementary to consider the lifetimes of features in the photosphere and corona. Schrijver et al. (1997) did a study of the evolution of the magnetic field in quiet sun areas and found that as much flux is cancelled as is present in quiet-network elements of the photosphere every 1.5 to 3 days, implying a timescale of $\approx$ 40 hours. Since the corona is driven by the photospheric magnetic field (which is in turn driven by the motions of the solar convective zone), and any single brightening can in general be associated with a *pair* of opposite-polarity flux concentrations, this implies we should see lifetimes of structures in the quiet corona on the order of $\lesssim$ 20 hours. Lifetimes significantly longer than this (stable, long-lived coronal brightenings in the presence of a continuously evolving magnetic field) would require either some form of continuous reconnection taking place at the loop footpoints, or for the magnetic features to be relatively stable and long-lived. Golub, Krieger, & Vaiana (1976a) investigated the lifetime of X-ray bright points with *Skylab* data and found a distribution heavily weighted towards short lifetimes on the order of hours. This result supports the notion of comparable timescales in the photospheric magnetic field and the corona.

In § 3.5 we compare length- and time-scales of the photospheric magnetic field to typical loop lengths in the 1 MK solar corona through both direct (manual) measurement from the data and also via auto- and cross-correlation analysis. Our observations show a close relationship between variation in coronal brightenings and the evolution of magnetic bipoles in the photosphere. We suggest it should be possible to find a statistical connection between the two; e.g. a common scale size and comparable lifetimes of magnetic features in both domains of the solar atmosphere. Simultaneously this observation provides a golden opportunity to explore the relationships between the timescales of magnetic features in the solar photosphere and the evolution of loops in the solar corona. We conclude that the quiet solar corona evolves on timescales comparable to timescales in the magnetic field. The observations indicate the quiet corona is undergoing continuous evolution and reconnection subject to the relative motion of flux concentrations in the underlying photosphere.

3.1.2 Coronal Heating Mechanisms.

Proposed mechanisms for energy transport into the corona are generally resolved into acoustic and magnetic phenomena (c.f. Narain & Ulmschneider (1996) for a review of heating mechanisms). Magnetic heating has been suggested as a leading contender for heating the solar corona as the brightest parts of the X-ray corona tend to occur in regions of enhanced magnetic field (Vaiana et al. 1977; Acton 1996). Magnetic heating mechanisms may be broken down into two primary categories: alternating current (AC) heating (wave heating mechanisms), and direct current (DC) mechanisms (joule dissipation of currents and magnetic reconnection).

AC heating methods are often manifested in observations as a non-thermal broadening of spectral emission lines due to magnetic wave phenomena such as Alfvén waves (see, e.g., Antonucci 1989; Alexander & Mackinnon 1993). Others have searched for global magnetic resonances in time series analysis of soft x-ray coronal loops (McKenzie & Mullan 1997). Litwin & Rosner (1998) suggest that there are two widely disparate characteristic timescales associated with wave heating: a short timescale associated with the initial phase of a loop, on the order of a few sound-transit times, and a much longer timescale associated with a steady-state phase with a relatively constant heating rate — giving rise to both impulsive brightenings and long-lived coronal structures. Investigations into DC heating mechanisms often take the form of a search for the presence of possible heating agents at sites of enhanced emission. For example, one might look for enhanced coronal emission at sites of high vertical current density. Deloach et al. (1984) performed this exercise in ultraviolet wavelengths for the transition region and Metcalf et al. (1994) repeated the exercise in soft x-rays for the solar corona. No correlation was found between current and enhanced emission in either study. In contrast, Falconer et al. (1997) studied five active regions and found a strong correlation between the brightest x-ray emission and the most strongly sheared magnetic field (as measured in photospheric vector magnetograms) at the neutral line. Fisher et al. (1998) took this a step further and correlated x-ray luminosities to several measureable global magnetic quantities. The strongest correlation noted was between soft x-ray luminosity and the total unsigned magnetic flux $\Phi_{tot} \equiv \int dA|B_z|$, where $|B_z|$ represents the line of sight photospheric magnetic field (see also Schrijver 1987). There are two caveats, however: (a) The correlation of a possible heating agent to a location of enhanced temperature does not establish that agent as responsible for the heating (Fisher et al. 1998), and (b) these methods only measure *global* quantities, not immeasureable local enhancements that may be more directly responsible for this heating.

The correlations found by Fisher et al. (1998) are compelling. If we assume the correspondence between Φ_{tot} and heating is real, it is then interesting to look for the manifestation of this heating mechanism. Many models of magnetic reconnection suggest the magnetic field accumulates stress in the form of non-potential (current-carrying) loop structures. The energy in the magnetic field in excess of a potential (zero-current) field is known as the *magnetic free energy* of the magnetic field. This energy is available for heating the corona when some pathway is found to liberate it from the magnetic field. A number of theories exist that describe possible mechanisms for the storage and eventual release of free energy into the corona. We consider two theories of coronal heating and compare the respective qualitative predictions to observations in section 3.7.

Parker (1983a, 1983b) argues that energy input into the coronal is a natural consequence of the motions of the photospheric magnetic field. Flux tubes are braided about each other by the random walk of the photospheric footpoints. The dissipation of this braiding transfers the work done by the footpoints (which in turn was done by the convective motions of the underlying plasma) into heat in the corona. For a coronal active region with a typical length $L = 10^{10}$ cm and an energy output $P = 10^7$ ergs cm^{-2} s^{-1}, this implied a pitch angle in the braided flux tubes (where $\tan\theta = B_t/B$, B_t is the transverse field) of $\approx 20°$. Galsgaard & Nordlund (1996) studied this mechanism further and did a numerical simulation using the full set of MHD equations. Their study suggested that field lines reach a *braiding number* — the number of times two neighboring field lines may braid about each other — of order one before reconnection takes place. These events were found to take place very rapidly compared to the speed of the driving motions, diminishing the degree of braiding. The source of heating will then be either along the current sheet (or, perhaps more accurately, a current *thread*) separating the braided loops or interior to a twisted loop that has reconnected. The net result will be that the source of heating (the current sheet) will be within or adjacent to the magnetic flux tube and any brightening will occur along the length of the loop. Localized heating in the loop will be conducted along the magnetic field lines.

This model is well-suited to describing the evolution of an ensemble of loops moving in close proximity to one another, but does not easily abstract to the case where additional photospheric footpoints approach, merge or cancel in neighboring proximity. Observations of the quiet corona in relation to the photospheric flux concentrations show a process of constant reconnection between opposite-polarity photospheric flux concentrations that approach and separate from one another. These footpoint motions often result in a very clear process of reconnection between otherwise unrelated magnetic concentrations (c.f. Schrijver et al. 1998). Furthermore, the Parker loop model does not specifically address the actual process of reconnection (though Galsgaard & Nordlund (1996) account for reconnection and heating via the development and resistive dissipation of a current sheet).

Longcope (1996) addresses this phenomena of brightening in reconnecting loops via a model termed the *Minimum Current Corona* (MCC). The MCC model attempts to describe the build-up of magnetic energy in a three-dimensional corona. The simplest example of this model may be described by two opposite-polarity photospheric flux concentrations P and N with flux $\psi_{\pm}$ separated by a distance d in an overlying background magnetic field $\mathbf{B}_0$. Magnetic field lines in this arrangement must fall into one of four domains: (1) Beginning at P and ending at N, (2) Beginning at P and ending at ∞, (3) Beginning at ∞ and ending at N and (4) purely background field beginning and ending at ∞. These four categories define domains Longcope (1996) refers to as P–N, P–∞, ∞–N and ∞–∞. The surfaces of these domains are called *separatrices.* In particular there are two surfaces Σ_A and Σ_B that are especially important. Σ_A contains all field lines that terminate at N, and Σ_B similarly encloses all field lines that terminate at P. The domain P–N simultaneously lies within both domains. The intersection of Σ_A and Σ_B is a single field line termed the *separator* σ.

In the MCC model, movement of the flux concentrations $\psi_{\pm}$ results in an induced current arising along a closed path defined by σ and a return path within the photosphere. All magnetic lines connecting the two flux concentrations P and N pass inside this loop. As the flux concentrations approach one another, a current is induced along the separator σ given by Faraday's law:

$$\frac{d\hat{\psi}}{dt} = -c \oint_{\sigma} E_{\parallel} dl, \tag{3.1}$$

where $\hat{\psi}$ represents the flux inside the domain P–N. This current along the separator prevents a change in flux.

When the current along σ achieves some *ad hoc* critical level it is supposed to be dissipated along the separator, and in that process the magnetic flux $\hat{\psi}$ is allowed to change. The heating mechanism takes place in proximity to the separator and should be clearly evident as a heating source at an angle $\Delta\phi$ with respect to the axis of the magnetic bipole (Longcope 1998). The released energy will disperse into those loops that connected across the separator at the time of current dissipation.

These two heating mechanisms (Parker loops and the MCC model) may well occur side by side and except in the most abstract sense represent different phenomena in the corona. Parker's model does not address the issue of two previously unassociated footpoints coming together. Similarly, Longcope's model does not address the relaxation of a twisted flux tube. It is an interesting exercise to look for signatures of both processes within the context of our dataset:

1. The MCC model suggests that the location of heating will be along the separator, which in general will be offset some angle $\Delta\phi$ to the bipole axis. The Parker Model predicts heating will occur along the length of the loop.

2. The MCC model predicts periodic heating via an *ad hoc* stick-slip mechanism. This might be apparent in observations as only random "flashes" along the separator, e.g. the separator would not be expected to radiate continuously. The Parker mechanism suggests a continuous process of nanoflaring along the loop may provide a nearly continuous source of heating.

3. There may be a clear delineation between converging and separating bipoles. The MCC theory dictates that as two photospheric flux concentrations P and

N approach, the coronal flux $\hat{\psi}$ connecting the two concentrations will tend to increase, and energy release along the separator will be deposited into loops closing across the separator σ. Similarly, loops reconnecting elsewhere will result in energy deposition into magnetic field lines connecting to domains other than P–N. Thus, the MCC model predicts that x-ray brightenings will favor brightenings associated with converging flux over emerging bipoles. The Parker model makes no statement on this issue, and little difference between emerging vs. cancelling bipoles would be expected.

3.2 Observations.

3.2.1 The Instrumentation.

Two space-borne instruments provided the data for this thesis project. Maps of the photospheric magnetic field were provided by the *Michelson Doppler Imager* (MDI, Scherrer et al. 1995). The primary mission of the MDI instrument is to measure velocity and continuum intensity at five wavelengths near the Ni I λ 6768 Å spectral line in order to measure solar oscillations in the photosphere. The MDI instrument is also able to observe the photospheric magnetic field. To this end, MDI has two modes for obtaining magnetograms. MDI obtains full-disk synoptic observations of the photospheric magnetic field every 96 minutes with 2 arcsec pixels ($\approx$ 2900 km resolution). MDI also operates in high-resolution mode using a different optical path that views a 10.5 $\times$ 10.5 arcmin field of view (0.6 arcsec pixels, $\approx$ 900 km resolution) centered on the central meridian and 160 arcsec north of disk center. In this mode, MDI can generate one magnetogram every 60 seconds. Both modes collect images with a 1024 $\times$ 1024 pixel CCD.

Observations of the solar chromosphere and corona are obtained with the *Extreme-ultraviolet Imaging Telescope* (EIT, Delaboudinière et al. 1995). The EIT instrument is a Ritchey-Chretien telescope using multilayer coated normal-incidence optics to image solar plasmas in selected extreme-ultraviolet (EUV) wavelengths (table 3.1). The telescope is divided into four quadrants, with each corresponding quadrant of the primary and secondary mirrors coated with complementary multilayers optimized for each wavelength. Wavelength discrimination is then made with a quadrant shutter to select one of the four quadrants. EIT full-resolution pixels are 2.59 arcsec, with a spatial resolution of $\approx$ 3800 km.

Table 3.1: EIT Bandpasses.

Wavelength	Ion	Peak Temperature
304 Å	He II	8.0×10^4 K
171 Å	Fe IX-X	1.3×10^6 K
195 Å	Fe XII	1.6×10^6 K
284 Å	Fe XV	2.0×10^6 K

These instruments both reside on the *Solar and Heliospheric Observatory* (SOHO, Domingo, Fleck, & Poland 1995). SOHO is a collaborative effort by the European Space Agency (ESA) and the National Aeronautics and Space Administration (NASA) designed to study the solar interior using techniques of helioseismology and to gain a better insight into the processes that form and heat the solar corona and the solar wind. The SOHO observatory was launched December 2, 1995 and placed into a halo orbit around the Sun-Earth L1 Lagrangian point where it continuously points at sun center.

3.2.2 The Observing Campaign.

EIT and MDI ran a high cadence joint observing campaign for a period of 85 hours from 10-Aug-1997 14:00 UT to 14-Aug-1997 03:00 UT. MDI high-resolution magnetograms were collected once per minute with occasional interruptions for full-disk magnetograms every 96 minutes, antenna handovers and other irregular, less frequent circumstances. The longest break in MDI magnetogram data spans three hours. EIT observed in the Fe XII channel (195 Å) with a temporal cadence of about 17 minutes. Periodic interruptions for the EIT synoptic program and other events are generally no more than one hour in duration.

The MDI field of view selected for this campaign spanned a region of 620 × 387 arcsec centered on the central meridian, ranging from lattitudes of 270 arcsec north of disk center to 670 arcsec north. The EIT field of view was over a 256 × 256 pixel field of view (660 × 660 arcsec) containing the MDI field of view (figure 3.1).

We generated seven-minute averages from the raw MDI data centered on the EIT exposure times and rebinned to 1.2 arcsec instrumental resolution. Conversion factors from the FITS headers (BSCALE and BZERO) (which trace back to instrument calibration) were used to convert raw data numbers to physical units. (The method of calibration may be found in Scherrer et al. 1995 and the calibration results are from P. H. Sherrer & T. D. Tarbell, private communication.) The conversion is a linear relation given by

$$B = 1.232 + 2.816(\mathrm{DN}) \tag{3.2}$$

where DN is the raw value from the FITS file and B is in units of gauss. The EIT Fe XII data was degridded, flat fielded, dark current subtracted, normalized to one second exposure rate and interpolated to 1.2 arcsecond pixels with the IDL *SolarSoft* package (Freeland & Handy 1998). The EIT data was flat-fielded and degridded with calibration data current as of 10-Nov-1997 (prior to the EIT CALROC calibration

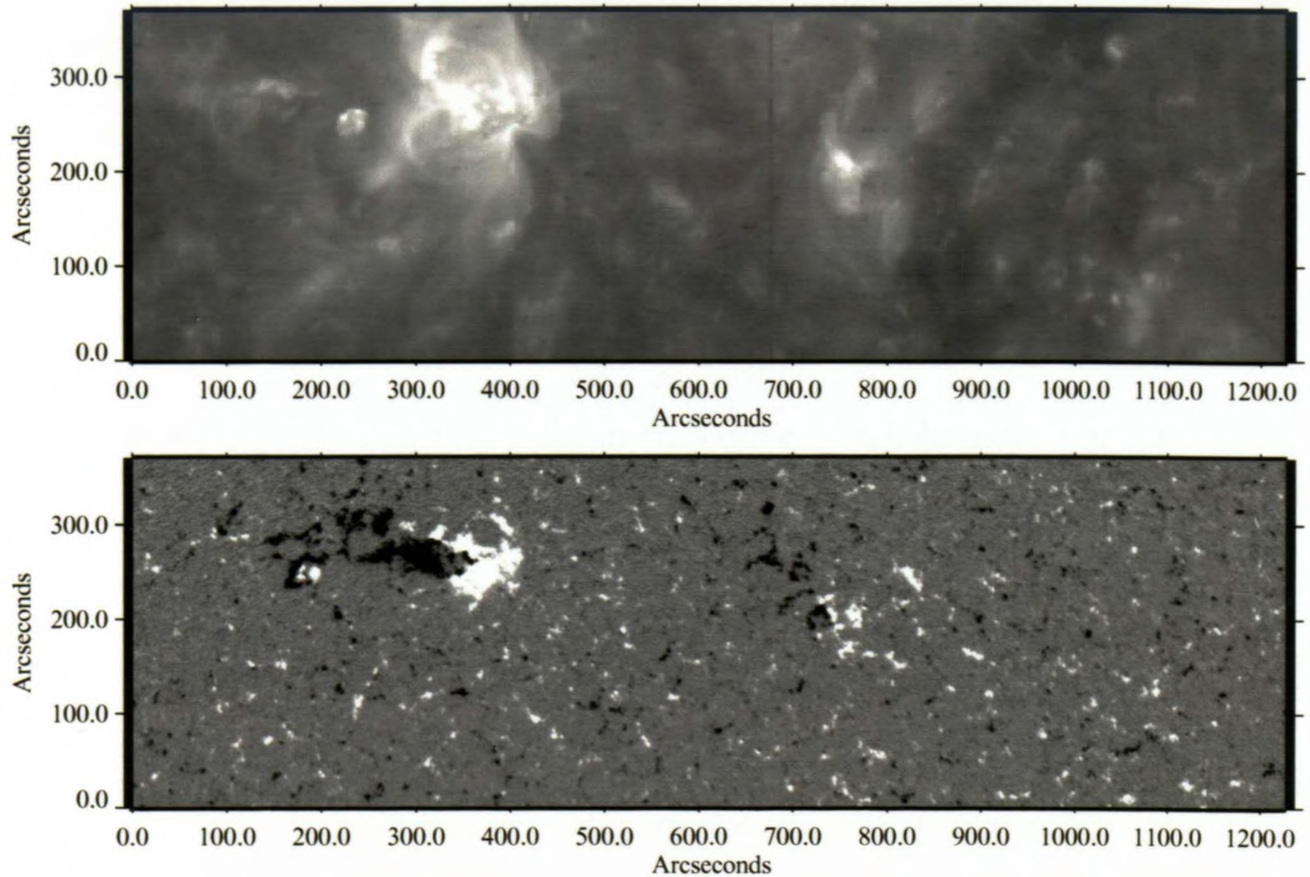

Figure 3.1: The composite field of view for the high-cadence coordinated time-lapse EIT-MDI observing campaign. The top image is the EIT Fe XII λ 195 Å field of view, displayed in units of logarithmic intensity. The bottom image is the corresponding MDI high-resolution view of the photospheric magnetic field scaled to ± 50 Gauss. The images were created by taking a slice from each image in the respective EIT and MDI movies, and splicing the slices together for this view. The EIT field of view was 256×256 full-resolution pixels (11 arcmin $\times$ 11 arcmin) and the MDI field of view was 1024×640 high-resolution MDI pixels (10.3×6.5 arcmin). The area common to the two instruments is shown in this figure. North is up, West is to the right.

flight). Both datasets were then coaligned and corrected for solar rotation.

3.3 EIT and MDI Movie Preparation.

The first EIT/MDI movie was made with Fe XII data displayed on a logarithmic scale and the MDI magnetograms contoured at ± 25 gauss levels, above the 2σ noise level (≈ 16 gauss) but low enough to show significant detail in the resulting movie. The movie was low contrast in many of the quiet sun regions and observations of the dimmest loop structures was problemmatic, and in numerous cases it was quite difficult to associate loop brightenings with the underlying photospheric magnetic field. To improve the contrast in the Fe XII images, the data was reprocessed with a high-pass filter to remove the diffuse background. The filter used was of the form

$$I_f = \frac{I_0 - I_s}{I_s} + C \times \text{smooth}\left(\log(I_0)\right) \tag{3.3}$$

where I_0 represents the raw image, I_s represents the smoothed image, I_f represents the filtered image. The smoothed term returns some context to the image with $C \sim 0.15$ and the smoothed image is a boxcar average over 5 arcsec. A comparison of the log-scaled and high-pass filtered images are shown in figure 3.2.

The filtered data are now displayed on a linear scale. The filtering process has increased the constrast sufficiently to bring out small (~ 5 arcsec), dim loops on a variety of size and length scales that were previously invisible (or nearly so) against the background haze. This filter works well not only on quiet regions, where it is

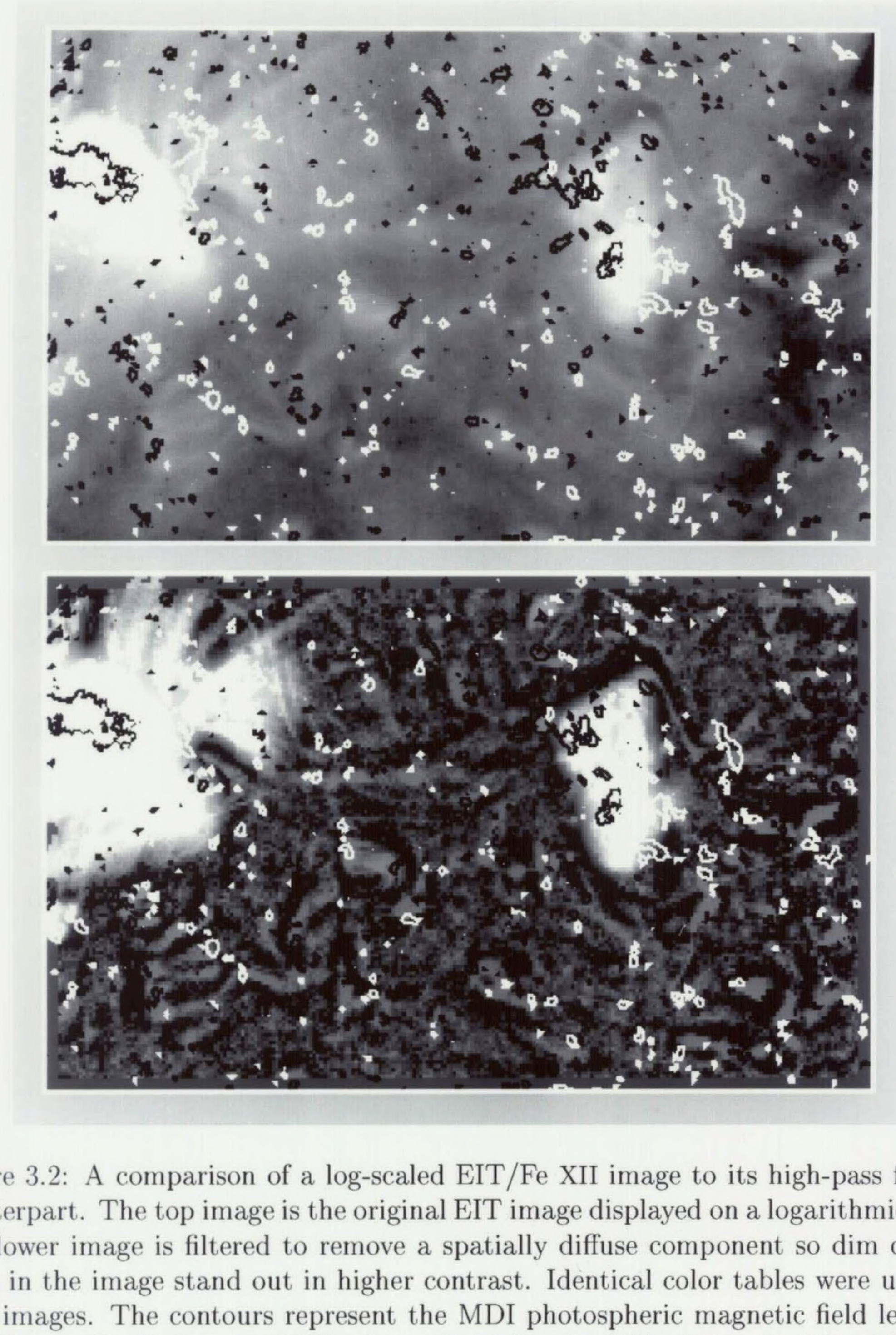

Figure 3.2: A comparison of a log-scaled EIT/Fe XII image to its high-pass filtered counterpart. The top image is the original EIT image displayed on a logarithmic scale. The lower image is filtered to remove a spatially diffuse component so dim coronal loops in the image stand out in higher contrast. Identical color tables were used for both images. The contours represent the MDI photospheric magnetic field levels at ±25 Gauss. North is up and West is to the right; the field of view is 450×280 Mm.

now significantly easier to pick out loops and see their connections to the underlying magnetic field, but also works especially well to isolate individual loops in the two bright expanding active regions (a topic beyond the scope of this work). Although the images have been flat-fielded and the CCD dark current has been subtracted, remnants of the CCD flat field and the filter support grids are visibly apparent in the reduced data. The filtered EIT movies are used for the analysis that follows unless stated otherwise.

3.4 Flux Emergence and Cancellation.

We find in general all flux emergences and cancellations above a threshold of 10^{18} Mx were associated with a noticeable brightening in the 1 MK corona. This is in contrast to the observations of Harvey (1997) who finds that no more than 25% of all emerging bipoles seen in NSO/Kitt Peak magnetograms result in brightenings visible in SXT. The higher density of loops in our observation may be related to several effects. First, the Fe XII channel is looking at cooler plasma ($\approx 1.6 \times 10^6$ K in Fe XII vs. 2×10^6 K in SXT). Secondly, the high-pass filter allows us to see loops hidden in the diffuse structure that would not be observed otherwise. On the smallest spatial scales and at the lowest intensities, these loops often have no counterpart in the more energetic SXT images.

Emerging loop structures were first visible in the corona when the flux tube separation reached 4500-8500 km and remained visible for typically 5-12 hours after the initial brightening before fading or reconnecting to other preexisting flux concentrations. These reconnections are generally manifested as a gradual shift in brightness between the initial pair of footpoints and the new connection to the preexisting concentrations. These expanding loop systems reached a maximum footpoint separation of about 14 Mm (c.f. figure 3.3). At this distance, the flux concentrations at the footpoints tended to merge with other, like-polarity flux concentrations and then reconnect to more distant concentrations. We observed no emerging concentrations expanding to significantly greater distances. In many cases emerging flux pairs had reconnected to neighboring pre-existing flux concentrations before separating enough for the connecting loop to reach coronal heights and emit in the Fe XII line.

A survey of the maximum footpoint separation seen in the EIT/MDI movie is shown in figure 3.3. Emerging (cancelling) regions in the movie were followed to their maximum separation forward (backward) in time. The number of observations was limited by the size of the instrumental field of view. In many cases it was not possible to observe the evolution of loop structures for the lifetime of the loop. The most frequent maximum length was ≈ 14 Mm, slightly shorter than the average supergranule diameter of 14–18 Mm (Hagenaar, Schrijver, & Title 1997). The average maximum length was ≈ 18 Mm.

Cancelling magnetic flux tended to connect at an average footpoint separation of 14 Mm before converging and disappearing from the coronal images. Cancelling features disappeared from the EIT images at a separation of 4-7 Mm. There were cases where the opposing flux concentrations at the loop footpoints appeared to be

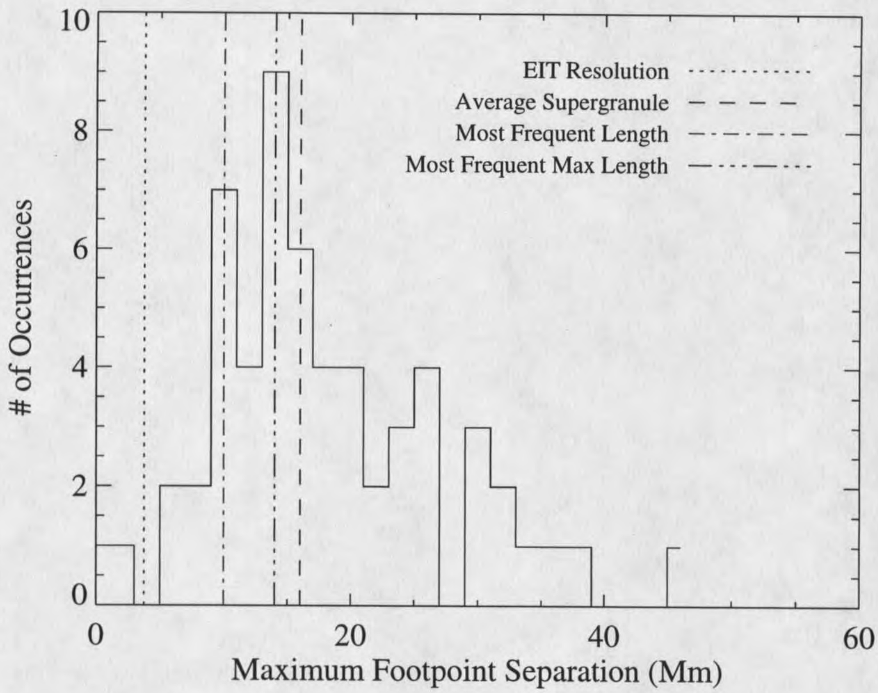

Figure 3.3: Maximum footpoint separations seen for emerging and cancelling flux and their coronal loop counterparts in quiet sun. Also indicated on the histgram is the limiting resolution of the EIT instrument, the most occuring length of footpoint separations from figure 3.6 and the average supergranule diameter from Hagenaar et al. (1997). The data point that falls below EIT resolution is a result of the loops blooming in the corona over a projected area larger than that of the photospheric footpoints.

in contact before the loop disappeared from the Fe XII channel, but the centroids of the magnetic footpoints were still separated by ≥ 4 Mm. This minimum separation may be a side effect arising from two possibilities: (a) we are approaching the spatial resolution of the EIT instrument, and (b) the magnetic loops must separate sufficiently to reach coronal heights before they are able to become hot enough to radiate in the Fe XII line. If we assume the loops are approximately semicircular in shape, this observation suggests the loops must reach a height of ~ 3 Mm before this condition occurs.

Emerging and cancelling flux concentrations tend to only remain (or become) connected while at a distance equal to or shorter than about one supergranule diameter, ≈ 16 Mm (Hagenaar, Schrijver, & Title 1997). The flux concentrations tend to emerge, spread apart, coalesce (or cancel) with other flux concentrations and then reconnect to more distant (or closer) opposite-polarity concentrations of similar strengths. In one particular case, a collection of emerging concentrations drifted about until the positive flux concentrations began to collect in a small region. This ensemble of positive flux concentrations were initially spread over ≈ 30 Mm and were connected to points approximately 20 Mm distant. As the positive flux concentrations began to merge, they reconnected several times to a number of negative flux concentrations over the course of 30 hours. They then coalesced into one flux element ≈ 14 Mm in diameter and reconnected to the negative pole of a large active region 110 Mm distant (figure 3.4). The total absolute value of the magnetic flux at the isolated pole of this loop at reconnection was $\approx 2 \times 10^{20}$ Mx, two orders of magnitude greater than typical quiet sun flux concentrations (Schrijver et al. 1997). This reconnection can be seen to have a distinct effect on the magnetic configuration of the active region, although it is nearly out of the field of view by the time of reconnection. This particular example is an extreme version of a phenomena seen several times on smaller spatial scales.

In one case, a flux concentration was observed to be connected to a distant concentration while simultaneously cancelling against a neighboring opposite polarity bundle. No loop structure connecting these two cancelling polarities was evident in the Fe XII images. This suggests a reconnection process between the loop footpoints and neighboring magnetic flux occuring at chromospheric heights.

In general we never observed an emerging bipole to spread, reverse direction and then again cancel against itself, but instead the concentrations would emerge, separate, reconnect to other pre-existing flux and eventually cancel elsewhere. It then stands to reason that unequal cancelling flux concentrations are the rule, with only a small fraction of the examples in our study completely vanishing from the magnetograms.

We observed several phenomena germane to both emerging and cancelling flux. There were numerous cases in which the coronal brightening connecting two footpoints favored the footpoint containing the largest amount of flux, in that the brightening was most obvious over the larger footpoint. In our filtered images the loops often appeared to taper in diameter from one flux concentration to the other instead of forming a loop of constant diameter. From this dataset it is not possible to discern if

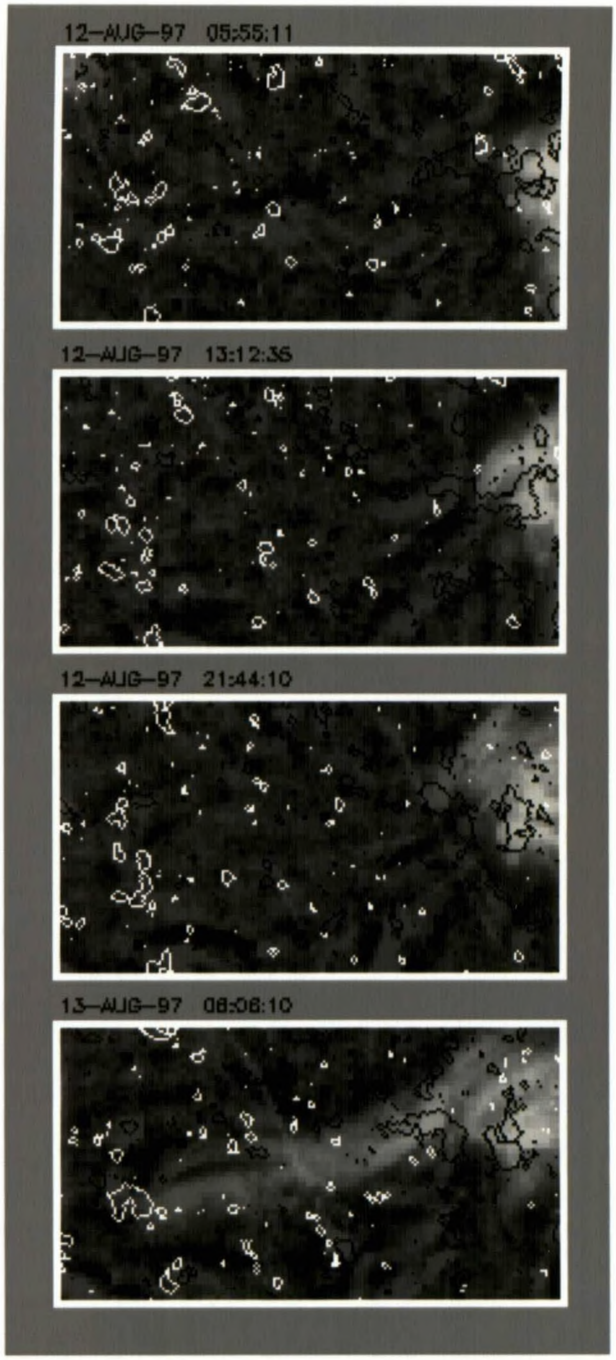

Figure 3.4: An illustration of flux collection and resultant magnetic reconnection in the corona. The positive flux concentration (left side of image, bottom frame) is about 14 Mm in diameter and has a total flux content of $\approx 2 \times 10^{20}$ Mx. The field of view is 450×280 Mm. The thin brightening drifting through the image (at center of bottom image, ≈ 25 degrees from vertical) is an artifact of the CCD flat-field.

the loops are tapering from one footpoint to the other or if part of the loop is simply not visible in our images. New results from the TRACE observatory show Fe XII loops in the corona with corresponding C IV 1550 Å footpoints ($\approx$ 100,000K) at or extremely near the photospheric footpoints (Schrijver, 1998, private communication).

In numerous cases, flux concentrations were observed to connect to multiple opposite-polarity concentrations. In some cases these multiple connections were evident when the loop structures first became visible in the corona, at other times the additional connections occurred after some relative motion of the participating flux concentrations. Another phenomenon observed was flux sources of one polarity connecting to a series of opposite polarity concentrations along a curved path (c.f. figure 3.5). We noted only a few isolated instances of this effect, but this phenomena became quite apparent in the process of collecting statistics for the sections that follow in this paper. It is possible this is a projection effect but in the instances we observed it appears that the loops are following a curved path leading to the opposite polarity. This can be explained by a potential field extrapolation. If the direction of the transverse field directly over one of the intermediate points along the loop is calculated, it would be found to lie in a direction tangent to the curve of the loop at that point. By this analysis, it is clear the loop structures should track the underlying footpoints.

In some cases we observed the brightenings and loop orientation to vary rapidly at the limit of our temporal resolution as, for example, two loops from one polarity concentration connected to two or more concentrations of opposite polarity some

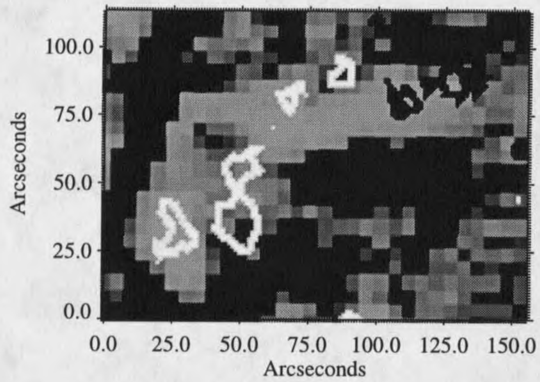

Figure 3.5: Multiple connections between polarities. In several examples the loops visible in Fe XII appear to follow a curved path passing over multiple concentrations (positive concentrations in this case). The structures seem to track the movement of the underlying footpoints. This phenomena can be modeled with a potential field. The Fe XII data was high-pass filtered to remove the diffuse background. The MDI data was overcontoured at ±25 Gauss levels. The loop in this figure appears to follow a path connecting the footpoints.

distance away. The loops appeared to vary in brightness in response to the movement of the underlying footpoints. This is in agreement with the observations of Harvey et al. (1994), who claim that the variability of bright points has little to do with the rate of magnetic flux change in the underlying magnetic structure but instead has to do with the relative motion of those structures. In most cases the loops appear to evolve, twist and wiggle rapidly in response to this footpoint motion. Coronal loop structures are also observed to deform and stretch in response to the evolution of the neighboring magnetic field. The observed motion is dependent on the flux strength and proximity of the neighboring field, and connection to that is further dependent on any apparent connections that flux concentration has elsewhere. This motion appears to happen over time rather than an instantaneous accomodating response to changes in neighboring flux concentrations. Rather, it evolves in a smooth manner at a pace consistent with the speed of evolution and strength of the neighboring field.

We never observed emerging regions to expand to distances in excess of about one supergranule diameter, but the mere existence of many loops in various stages of development on scales greater than this all over the quiet sun implies this discontinuous process is occuring on a continuous basis. When a sufficient quantity of flux concentrations coalesce, the coronal magnetic field tends to restructure to adapt to these new boundary conditions. Flux concentrations of similar strengths tend to connect to other flux concentrations of similar strengths, whether that connection happens in the immediate neighborhood of the concentrations (as is typically seen in active regions with large opposite polarity flux concentrations in very close proximity), or at relatively larger distances as seen in the example presented in figure 3.4.

3.5 Length Scales and Magnetic Reconnection.

We now generalize beyond emerging and cancelling phenomena and consider all quiet sun brightenings visible in the Fe XII channel during this campaign. In § 3.4 we alluded to the existence of several *domains* of loop sizes present in the quiet corona. Loops that are larger than the average supergranule diameter are typically the product of merging flux concentrations at the photospheric level and corresponding reorganization of the coronal magnetic field. A snapshot of footpoint separation associated with coronal loops is shown in figure 3.6. These statistics were collected by measuring the footpoint separation for all coronal loops that could be clearly associated with opposite polarity footpoints from three quiet sun regions over the duration of this observing campaign. Three images (one each from the beginning and end and one near the middle of the observing campaign) were selected for this study to cover all quiet regions that passed through the field of view during this campaign.

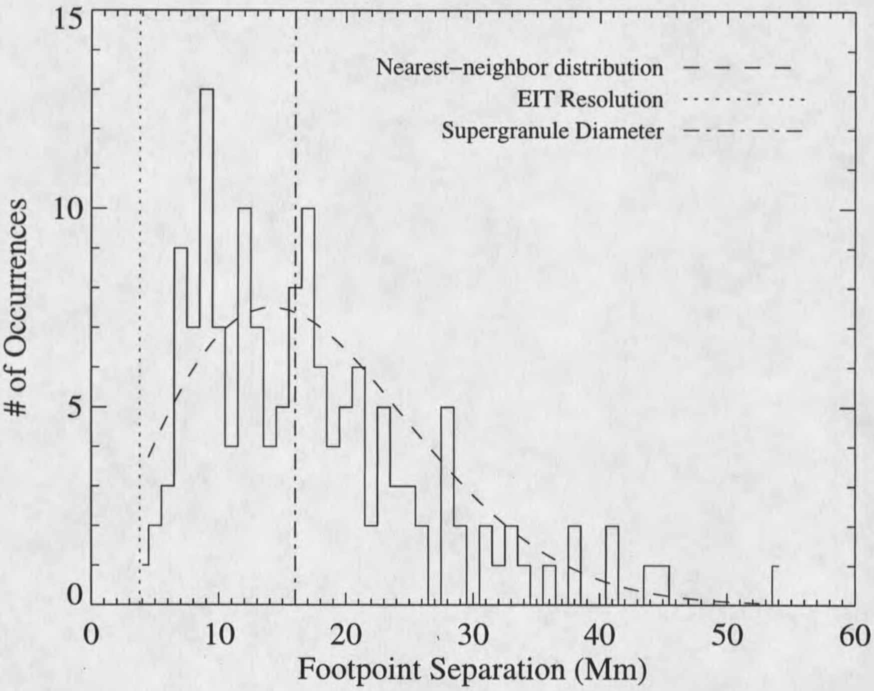

Figure 3.6: Distribution of coronal loop footpoint separations for loops visible in the EIT Fe XII (195 Å) Channel. The limiting resolution of EIT is 3800 km and the average supergranule diameter (from Hagenaar et al. 1997) is ≈ 16 Mm. The dashed line represents the analytic nearest-neighbor probability distribution for bipole cell sizes (e.g. one positive – negative flux pair per cell) of 1260 Mm^2. The most occurring value of the distribution is ≈ 12 Mm, and the average value of this distribution is 18 Mm.

This figure shows a distribution with a maximum value (the most frequently occurring length) of $\approx$ 12 Mm and a mean of 18 Mm. There is a cutoff at 3800 km (2.59 arcsec) at the limiting resolution of EIT full-resolution pixels. Quiet region loops with footpoint separations $\gtrsim$ 35 Mm are generally dimmer and more difficult to see against the diffuse background (c.f. Rosner, Tucker, & Vaiana 1978, Klimchuk 1992 for a discussion of loop models). Loop structures were excluded from this distribution if it was not possible to unambiguously associate a pair of opposite-polarity footpoints with the coronal brightening. Numerous examples of brightenings over like-polarity footpoints were evident, as well as loop brightenings that originated at one footpoint and then faded into the background.

This distribution of loop lengths (or, actually, photospheric footpoint separations) may be modeled analytically. If one assumes a random distribution of magnetic flux concentrations of one polarity and then places a flux element of the opposite polarity in this field, then the probability distribution $\mathcal{P}(r)$ describing the distance to the nearest neighbor is given by (Kendall & Moran 1963)

$$\mathcal{P}(r)dr = 2\lambda\pi r e^{-\lambda\pi r^2} dr \tag{3.4}$$

where r is the radial distance and λ is the density of points on the plane ($\lambda = 1/S$; S has units of area). This function was fit to the distribution with λ as the free parameter and the chi-square test was used to evaluate the goodness of fit.

The best fit (lowest χ^2) was given by $S = 1/\lambda = 1260$ Mm^2. To test if this analytical fit agrees with the distribution, the two quantities were compared via the

Kolmogorov-Smirnov (K-S) statistical test (Press et al. 1992). The significance level of equation 3.4 to the data found by the K-S test is found to be 0.159, which means that this distribution is only significant at the 16% level. Figure 3.6 shows a compelling fit but it is apparent that it does not completely describe the distribution. This are several possible explanations for this: recall that coronal loops do not always satisfy a nearest-neighbor relationship with the underlying magnetic footpoints, and also note that the photospheric distribution is not a perfect random distribution of points as this method would imply. Schrijver et al. (1997) fit the supergranular lanes to a Voronoi tesselation which suggests the magnetic elements tend to collect in a mesh of concentrations instead of being randomly distributed across the photosphere.

The area S actually encloses a *pair* of opposite polarity flux concentrations, so the area per flux concentration is half of this value or 630 Mm^2. Hagenaar, Schrijver, & Title (1997) measured the distribution of cell sizes in the chromospheric network and found that with a spatial smoothing of 7.7 Mm, the mean area $\overline{S}$ in quiet network was $\approx$ 610 Mm^2, in very close agreement with our observation. Some caution is appropriate here. While Hagenaar, Schrijver, & Title (1997) measured the geometry in the chromospheric network, for purposes of comparison between the coronal structures and the underlying magnetic field we have implicitly made the assumption that there will be one magnetic concentration for every network cell. Also, if the cell diameter is to be directly compared to the footpoint separation, that assumes magnetic field concentrations will always preferentially connect to nearest-neighbor opposite polarity distributions. Comparisons of EIT Fe XII loops to illustrations of nearest-neighbors in MDI magnetograms show that this is in general not usually the case (Hagenaar 1998, private communication). Comparison of the magnetograms to their coronal loop counterparts shows that loop structures have a tendency to connect magnetic concentrations of similar flux intensity.

Schrijver et al. (1997) measured the number density of flux concentrations in quiet chromospheric network. Their study showed that histograms of the frequency of flux concentrations with a given core flux content could be modeled by an exponential over the range 10^{18} to 5×10^{18}, e.g.

$$n = n_0 \exp\left(-\frac{\Phi}{\Phi_0}\right) \tag{3.5}$$

where n_0 and Φ_0 are constants, Φ is the threshold flux level and n is the number density of photospheric flux concentrations. The slope of the exponential $\Phi_0 \approx 3 \times 10^{18}$ Mx, which then implies the average total flux per concentration was found to be $\langle\Phi\rangle = \Phi_0 \approx 3 \times 10^{18}$ Mx. We then correlated the footpoint separation evident in the MDI magnetograms to the flux intensity in the footpoints (figure 3.7), using the high-pass filtered Fe XII images to show connectivity between the footpoints. The centroids of the footpoints were used to determine the separation, and the flux intensity was calculated as the integral of the flux over an area described by the 25 gauss contours of the footpoints in the magnetograms. Presumably the flux in the loop is no greater than that in the weakest footpoint, so the footpoint with the least amount of flux was used in this correlation. There is significant scatter in the correlation, but a

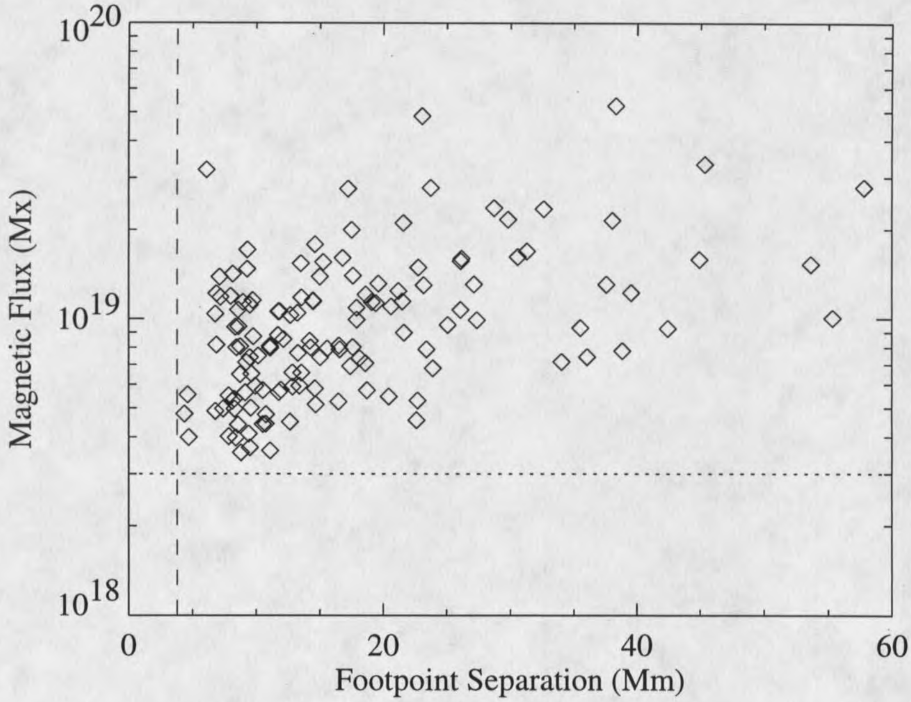

Figure 3.7: The footpoint separation of coronal brightenings in EIT Fe XII vs. the magnetic flux concentration in one footpoint. The flux was found by integrating the flux over an area defined by the ±25 gauss contour lines, and the flux from the smaller of the two concentrations was used for this figure. The dotted line is the average flux concentration found by Shrijver et al. (1997), and the dashed line is the limiting EIT resolution, 3.8 Mm.

few observations are evident. First, it is apparent that in order to see a brightening in the EIT Fe XII images, the flux in the loop must satisfy $|\Phi| \gtrsim 3 \times 10^{18}$ gauss. It is also evident that if the footpoint separation is sufficiently large ($\gtrsim$ 35 Mm), then more flux is required to connect the footpoints (the minimum value approaches 10^{19} Mx for separations $\gtrsim$ 40 Mm). Similarly, there is also a second trend for large flux concentrations to connect at greater distances. When flux concentrations merge and form larger concentrations, they are then able to reconnect to flux concentrations of similar strength at a wider range of distances, ranging from immediate neighbors (at distances of $\lesssim$ 10 Mm) to far-reaching concentrations at distances of $>$ 55 Mm. The strongest footpoints can be noted to connect to opposite polarity footpoints at any distance shown in the figure.

Hagenaar (1998, private communication) calculated the relationship between threshold flux levels and the resulting separation of flux concentrations based on the quiet sun data used elsewhere in this paper (figure 3.8). The MDI data was smoothed with a 1.2" gaussian, then flux concentrations that exceeded the two-sigma noise level (14 gauss) were selected for analysis. The density of points was calculated based on only counting those flux concentrations of magnitude greater than the threshold flux level. Based on the average cell diameter of 18 Mm from figure 3.6, this figure predicts a minimum footpoint flux concentration of $\approx 2 \times 10^{18}$ Mx in the loop. This is comparable to the minumum flux concentration of $\approx 3.5 \times 10^{18}$ Mx in figure 3.7.

Another technique for evaluating the relationship between loop footpoint separation and magnetic flux intensity is to integrate all unsigned flux in the region of

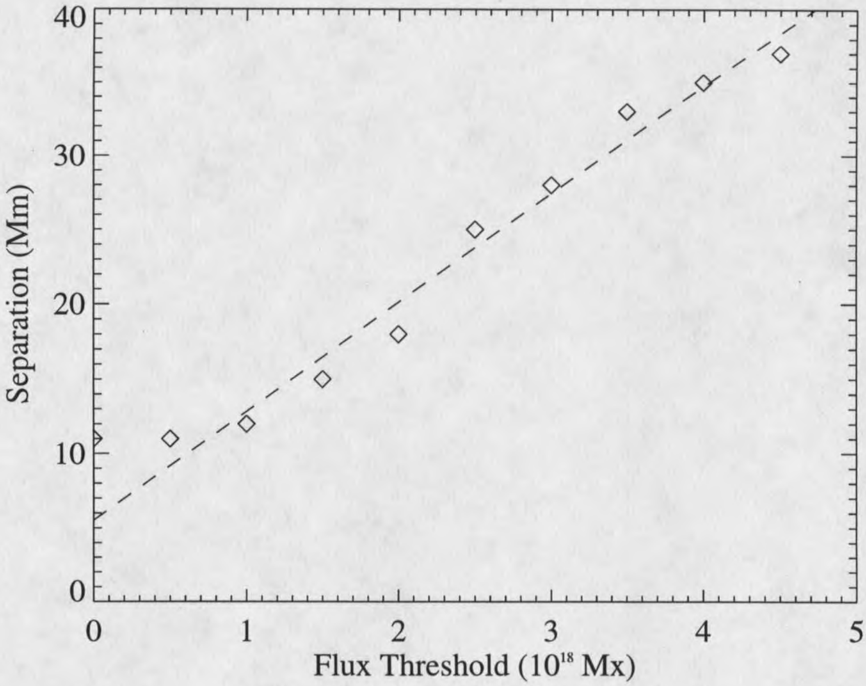

Figure 3.8: The relationship between threshold flux levels and separation between flux concentrations. MDI magnetograms were smoothed with a 1.2" gaussian, then flux concentrations that were above the MDI two-sigma noise level (14 gauss) were counted. Flux concentrations greater than the threshold value were used to calculate the density of points and in turn the average cell diameter of the concentrations. The rolloff below 1.5×10^{18} Mx is due to the selection process used in the flux concentration identification algorithm. Data courtesy H. J. Hagenaar.

the coronal brightening. Schrijver et al. (1998) calculated the flux as all flux above the two-sigma noise level ($\sigma = 7$ gauss) in a circle of diameter 27,000 km, under the assumption that the loop is affected by *all* flux in nearby proximity to the coronal brightening. This assumption is bolstered by the results of Fisher et al. (1998), who correlated global properties of vector magnetograms from the University of Hawaii's Mees Solar Observatory and found a very good correlation between X-ray luminosity over the entire active region and the total unsigned magnetic flux $\Phi_{tot} \equiv \int dA|B_z|$. In figure 3.9 we integrate over the area bounded by the loop brightening visible in the filtered Fe XII images and the coronal loop footpoints evident in MDI and see a similar correlation between these two quantities. This study is looking at flux concentrations and loop sizes much smaller than the active regions discussed by Fisher et al., but we reach a similar conclusion.

In figure 3.10 we compare the total unsigned flux under the loop to the total integrated intensity of the loop in Fe XII. This agrees with the work of Fisher et al. (1998) and is in agreement with the theoretical predictions of Longcope (1996), who predicts a qualitative variation of the luminosity with Φ_{tot}. This correlation is quite linear and is an extension to the analysis of Schrijver (1990) who suggested a power law fit of $L \sim \Phi_{tot}^{1.0}$ for a 1 MK corona for large-scale magnetic fields.

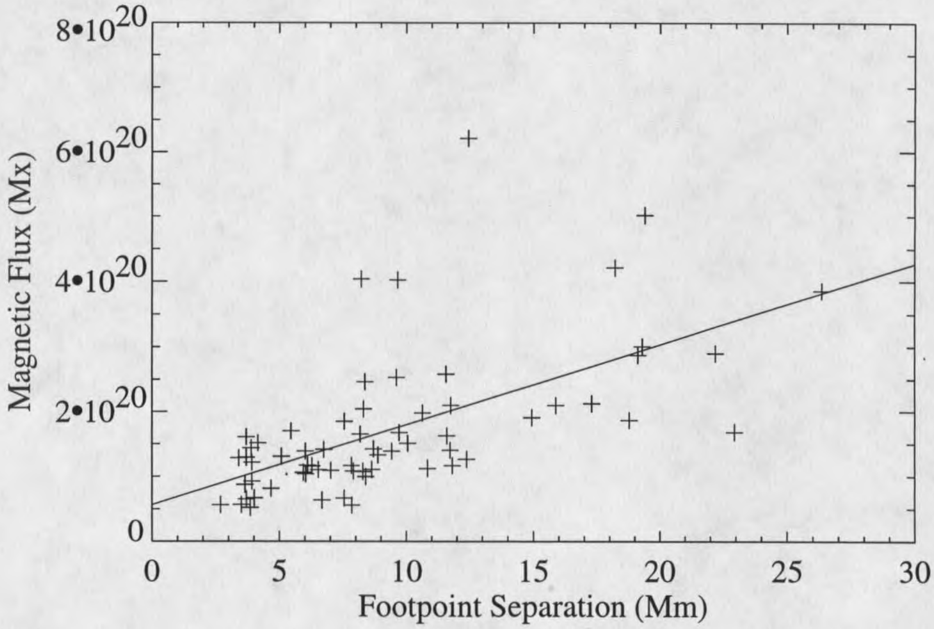

Figure 3.9: Footpoint separation versus total integrated unsigned magnetic flux. The footpoint separation was determined by the centroids of the magnetic flux concentrations, and the magnetic flux is the integral of the total flux defined by the projected area of the brightening in the Fe XII images and the loop footpoints.

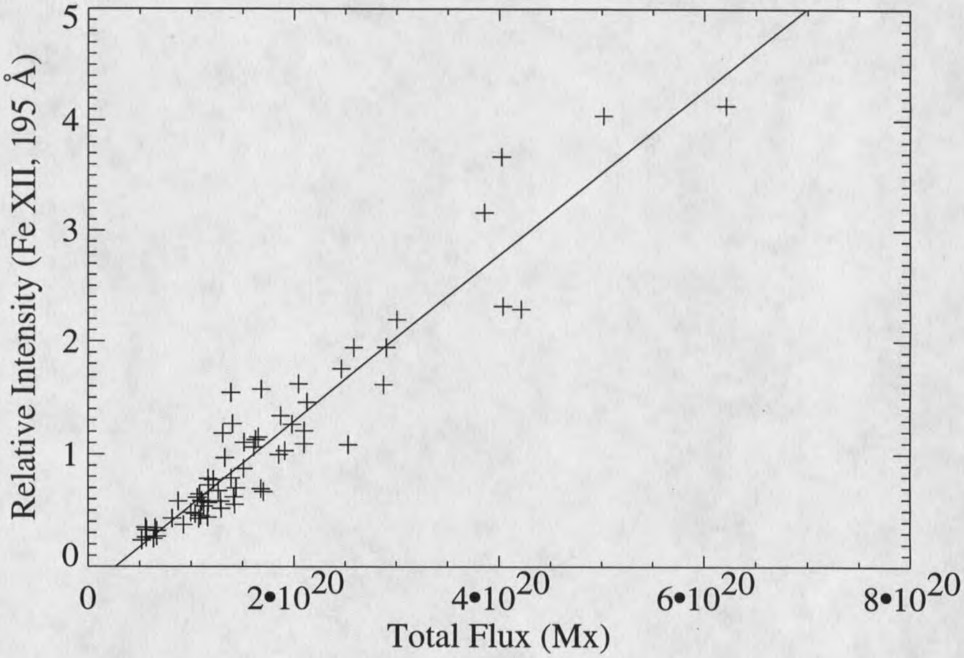

Figure 3.10: Relationship between integrated unsigned photospheric magnetic flux and total Fe XII loop intensity. The region of integration was chosen by selection a region surrounding the brightening visible in EIT and also including the footpoints as observed by MDI.

3.6 Autocorrelation Measurements.

Whereas the previous method of measuring the size and separation of coronal loops was done fairly directly, i.e. measured by hand directly from the data, it is biased by the ability of the observer to see the connections and accurately measure the distances involved. An alternative method that removes part of this bias at the expense of adding new ones is to perform an autocorrelation analysis of the EIT images.

Autocorrelation analysis is a technique for showing on a quantitative basis the similarities between two images. An analogy to this method is to overlay transparencies of two photographs on a light table. If there is a correlation between the two photographs (e.g. they are perhaps two separate pictures of a landscape) then there will be a definite position in which the overlap of features is very close and the transmitted light level will be at a maximum. As the transparencies are shifted over each other, the total light transmitted through the sandwich will begin to drop and approach some minimum (Leighton, Noyes, & Simon 1962; Simon & Leighton 1964; Mosher 1977). If there is some periodicity in the images then the transmitted light will again increase, in direct proportion to the correlation between the images. This technique is useful for measuring the scale sizes in an image (autocorrelation) and also for comparing two dissimilar images (cross correlation). The correlation function in two dimensions is given by

$$C(a,b) = \frac{\int (T_1(x,y) - \overline{T_1})(T_2(x+a,y+b) - \overline{T_2})dA}{(\int dA)\sigma_1\sigma_2} \tag{3.6}$$

where $C(a,b)$ is the correlation function, T_1 and T_2 are the intensities of the two images (or transmission of the film, as described above), $\overline{T_1}$ and $\overline{T_2}$ are the image mean intensities, a and b represent the *lag* between the two images, the standard deviation of the two images is given by σ_1 and σ_2 and the integrals are over the area of interest A. For identical images ($T_1 = T_2$) this is an autocorrelation function; when separate images are compared ($T_1 \neq T_2$) the result is a cross-correlation function.

This relation yields two useful pieces of information about the structure of the image. First, the full width at half-maximum (FWHM) is a measure of the "correlation distance" or the linear scale of the fluctuations. The central height of the function (for lag $a, b = 0$) is a measure of the r.m.s. fluctuation of the two images. If a plot of correlation vs. lag a or b is generated, the FWHM of that curve is a measure of the correlation distance along the respective axis.

It is apparent from the photograph analogy and equation 3.6 that this method favors the large-scale structures in the images, so the new bias in the measurement of coronal loop structures is that the final result will be weighted towards the larger structures. The correlation analysis that follows was limited to quiet sun regions to reduce this bias.

In figure 3.11 we show typical autocorrelation amplitudes in the linearly-scaled EIT Fe XII movie. Three quiet regions were chosen from the full field of view of the observation in an effort to mitigate effects from the large-scale loops connecting the two active regions. The autocorrelation curve was calculated from the linearly-scaled images over a lag of ± 60 Mm for each frame in the field of view. This array of

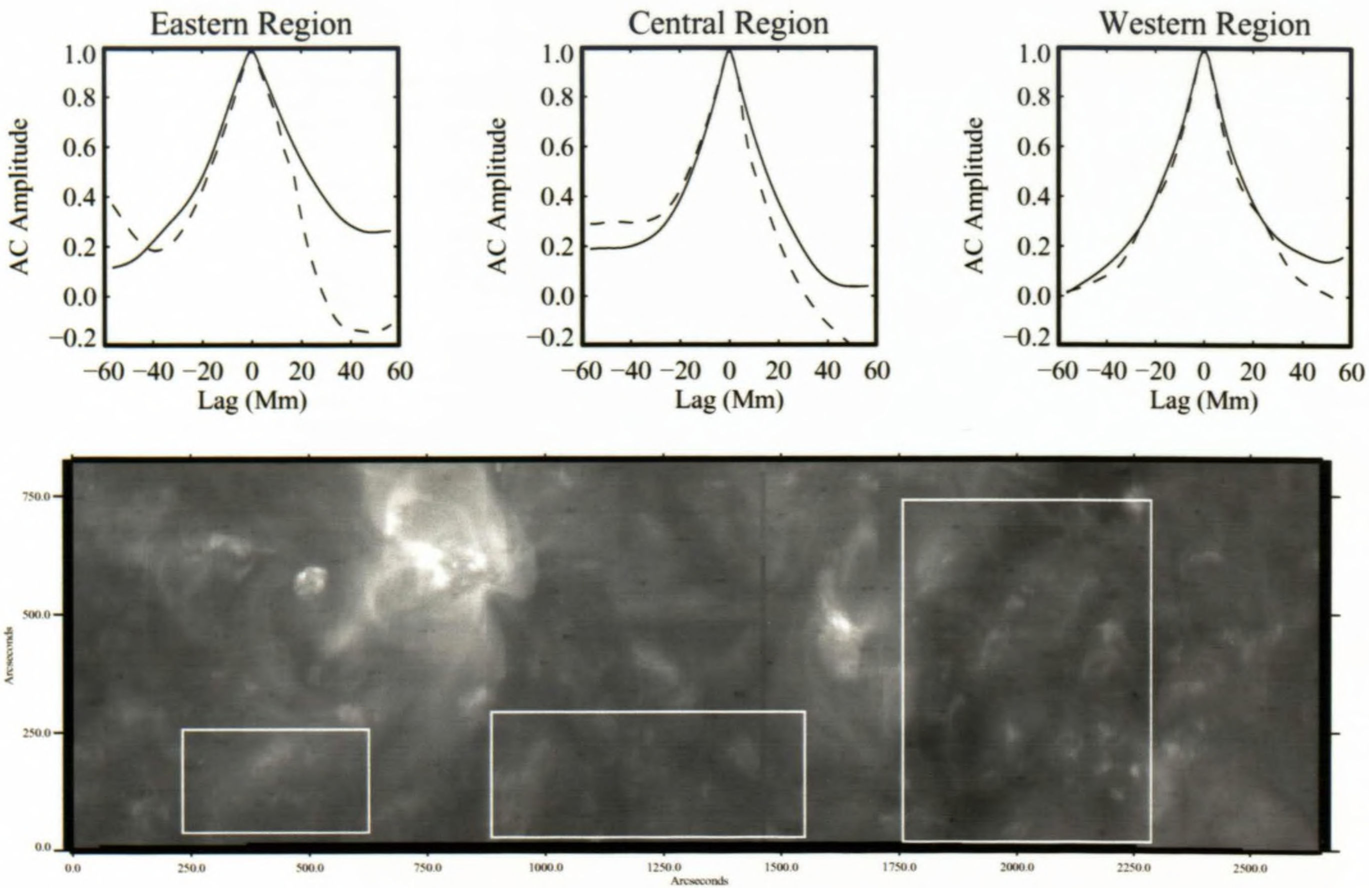

Figure 3.11: Averaged Fe XII autocorrelation curves. Solid lines are EW, dotted lines are NS. The autocorrelation graphs correspond to the three quiet regions outlined in the lower figure. The eastern region is averaged over 47 frames, the central region over 100 and the western region over 51 frames. A distinct variation between EW and NS is seen in the eastern region (and to a lesser extent the central region), due to large loops from the active region passing over the field of view. The Western region is least affected by these overlying loops and the similarity in correlation distances suggests the orientation of quiet sun brightenings is isotropic. The typical size scale (FWHM) is $\approx$ 26 Mm.

correlations was then averaged to yield the curves in figure 3.11. The anisotropy in N-S and E-W correlation in the eastern and central regions indicates these regions were affected by the presence of overlying loops. This is evident both in the movie and the averaged autocorrelation curves. The western region was free of this effect, and the correlation plot for this region suggests that quiet sun coronal brightenings are generally isotropic in their orientation.

The *a priori* assumption was that the loops would be biased towards an east-west orientation as is often seen in large active regions. However, aside from the influence of the large-scale active region loops, the autocorrelation curves show little difference in the N-S and E-W directions. It is possible that if the loops are about the size of a supergranule and are separated by a distance of about a supergranule, then the autocorrelation would be expected to be isotropic. However, if the majority of all concentrations shared a common orientation we would still predict a visible bias in the autocorrelation unless the orientation falls along a 45° angle to the two axes, as the coronal loops would tend to autocorrelate along their length in one axis (e.g., E-W) and across their width in the other axis (N-S). The present result is in qualitative agreement with inspection of the data by eye: there is no obvious bias in the orientation of small-scale loops.

This isotropy in loop orientation may have several plausible explanations. First, we note that the size of the magnetic flux concentrations found at the footpoints of the loops in this study are quite small, often on the order of 10^{18} Mx. As one progresses towards smaller flux concentrations, the Hale Polarity Law (Hale 1919) seems to apply less cleanly. Harvey-Angle (1993) (chapter 3) studied the orientation of active region loops and found that as the size of the region decreased, the orientation of the magnetic bipole beneath the region became less likely to align with a preferential rotation. The results here are an extension of Harvey's study. There are likely several phenomena in effect at these smaller sizes and domains. First, the smallest magnetic flux concentrations are more likely to be influenced by the motions of the sun's convective layer and hence will be subject to significant mixing and shifting before reaching the photosphere. Once at the surface, the flux concentrations are subject to constant shifting and subsequent reconnection to other flux concentrations, discussed qualitatively in § 3.4. Any preferential orientation of flux concentrations at emergence will be rapidly dispersed as the concentrations reconnect to other, randomly-oriented neighboring flux concentrations.

With a grasp on the size of coronal features, it is then useful to consider the lifetimes of coronal loops via cross-correlation. We compare a series of linearly-scaled images in time to the first image and plot the maximum correlation amplitude as a function of time (figure 3.12). This study used the same regions as were used for the autocorrelation method discussed previously, and the time domain of the graphs runs for the length of time each field of view was fully present in the images. The lifetime of the structures visible in the corona is measured as the amount of time necessary for the cross-correlation amplitude to drop to a factor of 0.5. We find the quiet 1MK corona has a timescale of nominally 12 hours and is completely decorrelated — retains no "memory" of its original configuration — in 20–25 hours, at which time the correlation begins to oscillate about the minimum value.

Based on these observations of the quiet corona, it is then instructive to attempt a similar study in the photospheric magnetic field. This is a significantly more difficult issue to address, as magnetic fields do not lend themselves to being autocorrelated. Rather than decorrelating over a distance comparable to a supergranule diameter or over the length of a coronal flux tube, the magnetic field is much more likely to decorrelate over the diameter of a flux concentration, often on the order of a few pixels in quiet sun. In an attempt to mitigate this difficulty, we create a polarity map from the MDI images (figure 3.13). Magnetograms from five hours of MDI observations were averaged to make the polarity pattern in the supergranular lanes more apparent. The result of this averaging process is shown at top in figure 3.13. The polarity map was created by smoothing the magnetogram over 6 arcsec and then setting the positive polarities to +1 and the negative polarities to −1. This smoothing process removes the small scale magnetic features ($\lesssim$ 3800 km, the scale dictated by EIT resolution) least likely to be involved in coronal brightenings and simultaneously enhances the magnetic patterns in the supergranular network. The corresponding polarity map is the lower illustration in figure 3.13.

This processed image was then autocorrelated. The entire MDI field of view was used for this calculation, including the active regions. The result of this autocorrelation is a scale size of 7.5 Mm, the FWHM of the autocorrelation amplitude (figure 3.14). This result is significantly smaller than the scale sizes we see in the coronal images, both in direct measurement and the autocorrelation results. Once

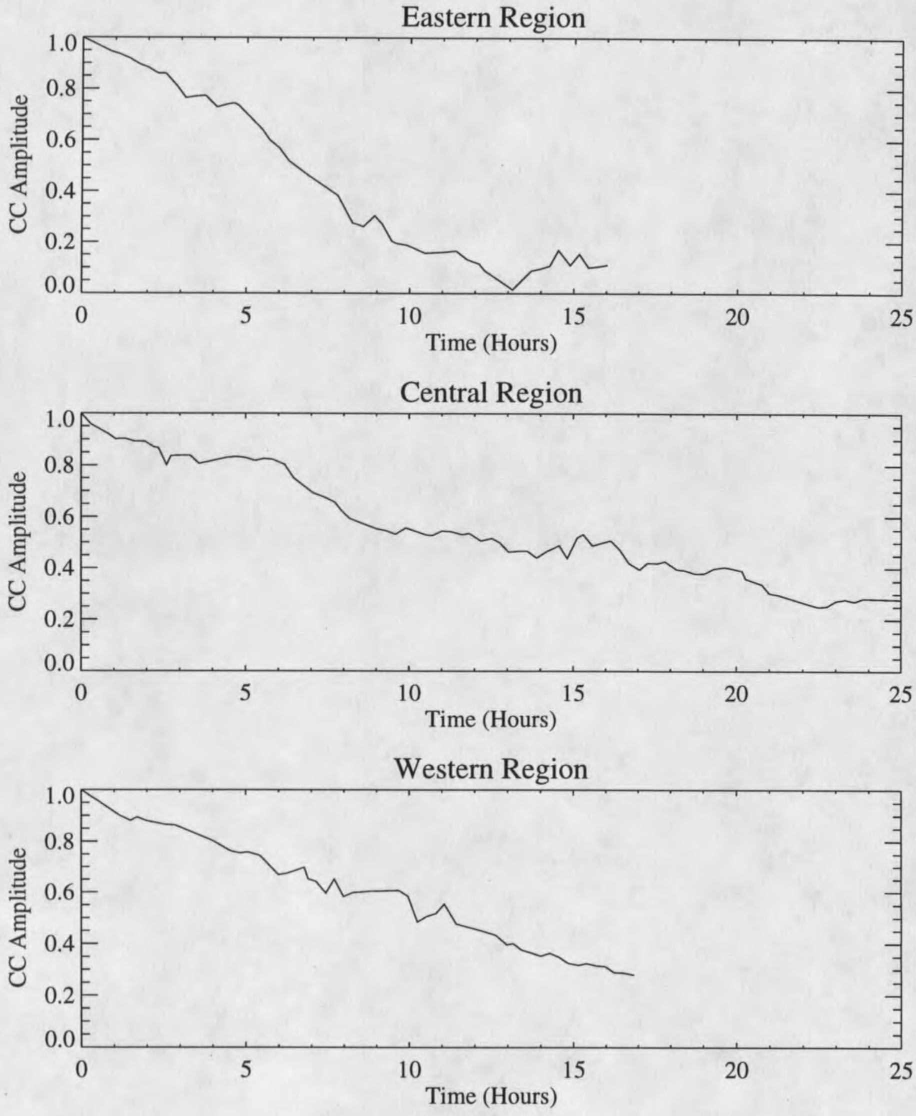

Figure 3.12: EIT/Fe XII crosscorrelation in the quiet corona in the same regions as figure 3.11. The top curve shows the greatest discrepancy in decorrelation bias due to the evolution of the large-scale loops emanating from the neighboring active region. The remaining two regions decorrelate in ≈ 12 hours.

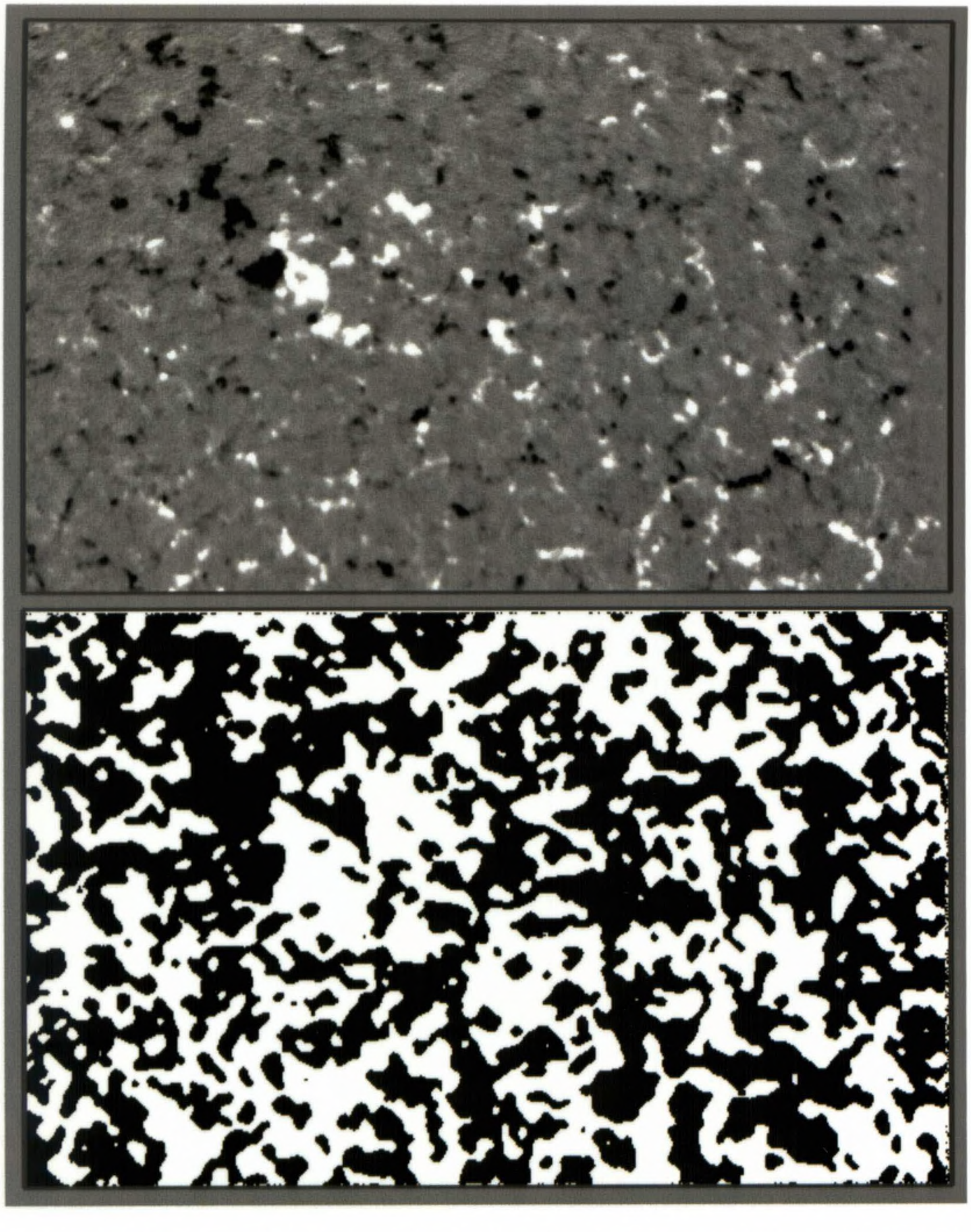

Figure 3.13: Characteristic magnetic field polarity pattern. The top image is an average of five hours of MDI magnetograms, one per minute, corrected for solar rotation. The bottom image is a polarity map, generated by smoothing the top image over 6 arcsec and then setting positive regions to +1 and negative regions to −1.

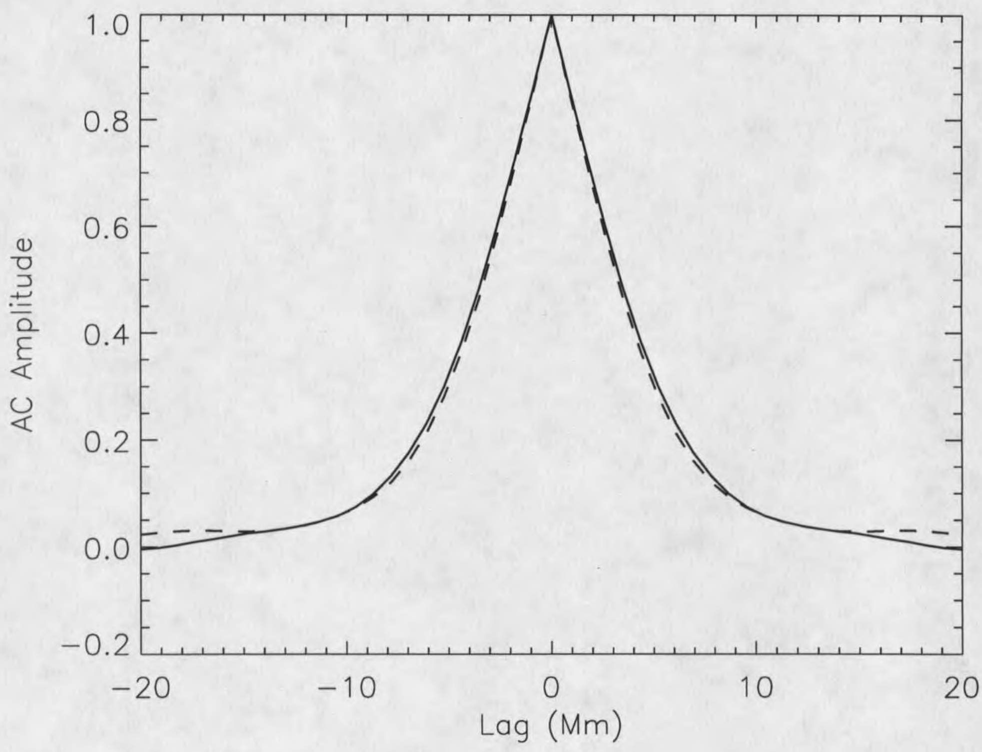

Figure 3.14: Autocorrelation amplitude of the photospheric magnetic field polarity pattern. Solid line is EW, dotted line is NS. The FWHM of the polarity map (the characteristic size of the flux elements) is ≈ 7.5 Mm.

again there is an apparent isotropy in the shape and size scale of magnetic phenomena in the solar photosphere, but the reasoning is somewhat different from that of the previous coronal arguments. If an instantaneous snapshot of the solar corona showed a arrangement of coronal loops all of footpoint separation d separated by a distance d, all oriented along a common axis, while there would be an anisotropy in the coronal loop correlation distance the underlying magnetic field would appear to be completely isotropic. Further complicating this issue is the fact (from § 3.5) that magnetic flux concentrations do not have any great tendency to connect to nearest neighbor opposing flux concentrations. It is not possible to address this issue based on correlation techniques.

3.7 Mechanisms of Bright Point Heating

3.7.1 Morphology of coronal brightenings

Parker (1983b) and Longcope (1996) propose two complementary methods of coronal heating via direct-current (DC) magnetic field dissipation (c.f. § 3.1.2). Parker argues that coronal heating is a natural extension of the motions of the convective zone giving rise to twisting and braiding of magnetic loops in the corona. These braided magnetic loops then periodically reconnect and relax into a potential field configuration, releasing the magnetic free energy in the form of heat which is then dissipated along the length of the loop. Longcope suggests a model of coronal heating in which the relative motion of opposite-polarity magnetic flux concentrations result in reconnection between these concentrations. As the flux concentrations move relative to one another, a current is induced along a closed path $\mathcal{C}$, composed of the *separator* σ and a return path in the photosphere between the two concentrations P and N, opposing any change in flux connecting P to N. When the current flowing in $\mathcal{C}$ reaches some *ad hoc* critical level, it is dissipated via anomalous resisitivity into the corona and the magnetic field between P and N is allowed to relax towards a current-free configuration. This model describes the minimum permissible current in the corona and is referred to as the *Minumum Current Corona* (MCC).

This model implies a number of morphological conditions that should be evident in solar observations. Perhaps the most obvious side-effect of this reconnection model is an angular discrepancy between the axes of the coronal brightening and the mag-

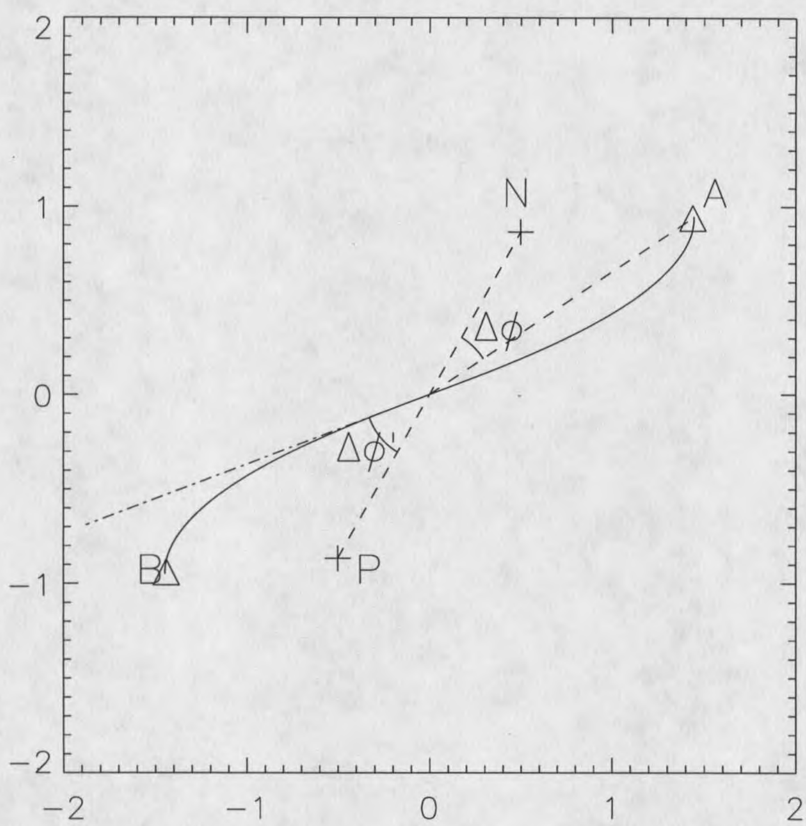

Figure 3.15: The separator field line AB, viewed from above, for a magnetic bipole. The axis of the bipole is shown as a dashed line, N and P represent the loop footpoints. Also shown are two definitions of the separator axis (dashed and broken) leading to two offset angles $\Delta\phi$ and $\Delta\phi'$. Figure courtesy D. W. Longcope.

netic footpoints (figure 3.15). In practice the brightening will be at an intermediate angle between the bipole axis and the background field $\mathbf{B}_0$, and it dependent on the relative strengths of $\mathbf{B}_0$, the magnetic footpoint fluxes $\psi_{\pm}$ and the footpoint separation. This offset angle has been observed in EUV images from a sounding rocket flight (Kankelborg et al. 1996), in selected soft X-ray images from the *Yohkoh*/SXT telescope (Longcope & Silva 1998), and in observations of EIT Fe XII bright points in comparison to the MDI photospheric magnetic field (Kankelborg 1998, private communication). This theory further predicts the footpoints of the apparent loop brightening will be at locations offset from the magnetic bipole footpoints, and the overall length of the loop will be slightly longer than the magnetic bipole (Longcope 1998).

Qualitative observations from the EIT Fe XII movie show brightenings that appear to fall along the axis connecting the photospheric magnetic footpoints. Furthermore, as the footpoints evolve and move in time the brightenings tend to shift from one pair of connections to another in a smooth transition as the boundary conditions at the photosphere change in time. This process is suggestive of a continuous Parker-like mechanism in which small-scale relaxations occur along the length of the loop, providing continuous energy input at what appears to be a continuous series of points along the loop. These continuous brightening methods are also indicative of some form of wave heating occuring in the loop which could provide the continuous energy input required to bring the loop brightness up to some steady state.

We also noted in § 3.4 we noted that all flux above a threshold of 10^{18} Mx were

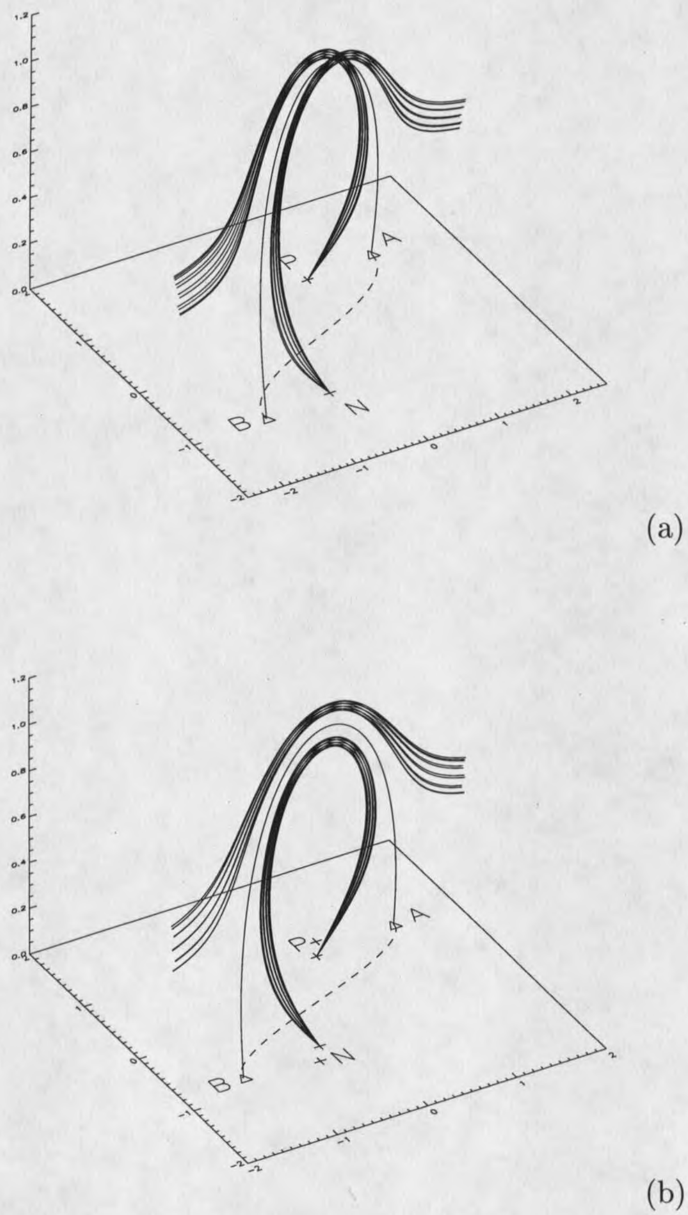

Figure 3.16: Field line orientation before and after reconnection across the separator. In (a), the magnetic concentrations P and N are approaching each other and an induced current develops along the separator A-B. Figure (b) is after the current has dissipated and reconnection has occurred. The energy stored in the separator current has dissipated into the loop now connecting P-N. Figure courtesy D. W. Longcope.

associated with a noticeable brightening in the corona. Longcope (1998) shows that for some relative orientations of the bipole axis in relation to the background magnetic field there will be no loop brightening. Since in § 3.5 it was determined that quiet sun coronal brightenings tend to be isotropic in orientation, and since presumably in quiet sun the orientation of $\mathbf{B}_0$ will also be isotropic, it is likely that in at least some subset of the cases MCC reconnection would not apply, but a brightening is still present. Another example of conditions in which MCC would not apply would be a situation in which the footpoints are stationary. A few examples of this are evident, and it is clear the loops are still being heated. The footpoints suggest some sort of twisting motion may be occuring, but it is difficult to tell from the magnetogram data.

We surmise that the most likely candidates for demonstrating heating along the separator axis would be magnetic flux concentrations converging and reconnecting from other sites. What we would expect from the MCC model is a brightening occurring along the separator between the concentrations. In general, however, we find very little evidence of this happening. The following is a typical scenario: two photospheric flux concentrations P and N (initially connected to other distant concentrations) approach one other in a random walk pattern in the photospheric network. As these two concentrations close to a distance where they begin to reconnect, there is a transition period as the magnetic flux reconnects from the old concentrations to the new ones, and coronal brightenings will be simultaneously visible between each of the footpoints P–N, P–∞ and N–∞ (where ∞ here represents the initial connections). Hence, both photospheric footpoints will simultaneously show brightenings in two separate sets of loops. The new connection P–N is manifested as a loop apparently linking the magnetic bipoles and there is little observational evidence to suggest that this brightening is taking place along the separator. The observational evidence most closely favors either some form of wave heating or the Parker loop heating model, but we are unable to (a) discuss the mechanism of Alfvén wave dissipation based on observations from our dataset or (b) note any significant twisting or braiding of the photospheric footpoints that would lead to the energy release described by Parker (1983b).

There are examples of brightenings that do not specifically show connectivity to the footpoints. For example, we see coronal brightenings in which the endpoints of the coronal brightenings do not show a perfect overlap with the footpoints in the magnetic field, or the brightenings shift relative to the footpoints. We expect to some extent this is an artifact of looking at structures near the resolution limit of EIT. In the quietest areas in the field of view for this observing campaign, we see a variety of brightenings that do not directly overlay the photospheric footpoints. There are other curious brightenings that seem to connect two like-polarity footpoints.

The Parker mechanism fares better against our observations, but as discussed in the introduction is unable to explain all possible forms of reconnection. What we see predominantly is a selection of coronal brightenings that apparently connect two (or more) opposite-polarity photospheric footpoints. The Parker mechanism does not address heating mechanisms arising from the translation of footpoints about the photosphere leading to reconnection in the corona, but instead requires the magnetic loops to either twist or braid themselves against neighboring loop structures. In the quiet sun features we find that the smallest visible structures are below the resolution of EIT and we are unable to comment on possible braiding mechanisms. A litmus test of the Parker mechanism would be a coronal loop that remains bright while the footpoints remain stationary. We do see isolated instances of this, where the footpoint separation remains constant for times on the order of hours, but the shape of the footpoints evolve and change. It is conceivable there is some twisting or braiding of magnetic field lines happening in these cases. Even in these examples where the footpoints remain stationary, the corona continues to move, vary in brightness and writhe in apparent response to the motion of other neighboring photospheric magnetic concentrations.

Since we do not see evidence of heating driven by induced currents along the separator, in light of the observations of others mentioned previously it is interesting to ponder why. Using standard loop models we can perform some simple thought experiments to see how long this heated plasma might be visible near the separator. Zwaan & Schrijver (1999) summarize these models to show that the *dynamical time scale* $\hat{t}_{L,d}$ for a loop (the time required for the pressure in a magnetic loop to equalize after a flaring event) may be given by

$$\hat{t}_{L,d} = \frac{L}{c_s} = 1.3 \frac{L_9}{\sqrt{T_6}} \text{ (minutes)}. \tag{3.7}$$

for a loop half-length L, sound speed c_s, and temperature T with L_9 representing units of 10^9 cm. For a typical quiet sun brightening we choose $L_9 \approx 0.1$ and for Fe XII loops $T_6 \approx 1.0$, yielding $\hat{t}_{L,d} \approx 6$ seconds. This energy can be radiated away in a time on the order of the *radiative time scale* $\hat{t}_{L,rad}$ given by

$$\hat{t}_{L,rad} = \frac{3n_e kT}{n_e^2 \mathcal{P}(T)} \approx 64\hat{t}_{L,d} \text{ (minutes)}, \tag{3.8}$$

with electron density n_e and a radiative loss curve $\mathcal{P}(T)$ approximated by $2{\cdot}10^{-23}T^{-1/2}$ erg cm^{-3}s^{-1}. For our $t_{L,d}$ we find the energy due to reconnection would be radiated away on a timescale $\hat{t}_{L,rad} \approx 6$ minutes.

Longcope (1998) predicts the interval between reconnection events Δt can be approximated by

$$\Delta t \simeq \left(\frac{1}{13}\right) \frac{\psi_0^{1/2}}{vB_0\Lambda(\theta)} \text{ (seconds)} \tag{3.9}$$

where θ is the critical current parameter, $\Lambda(x) = x \ln(256e^{-3}/|x|)$, $\psi_0 \approx 5 \times 10^{18}$ Mx, $B_0 \approx 10$ gauss and $\theta = 0.15$, yielding $\Delta t \approx 45$ minutes. Hence, a reconnecting bipole with these parameters should show visible brightening near the separator about 10% of the time. The cadence of the EIT observations (17 minutes) implies this separator brightening process would be manifested as occasional (typically only one frame) brightenings along the separator, not a continuous bright region.

Evidently, in any one single loop reconnection event one may not see a brightening occuring along the separator. In any given image, statistically some reconnection events should show a brightening along the separator. Observations, in general, do not support this conclusion (c.f. figure 3.17).

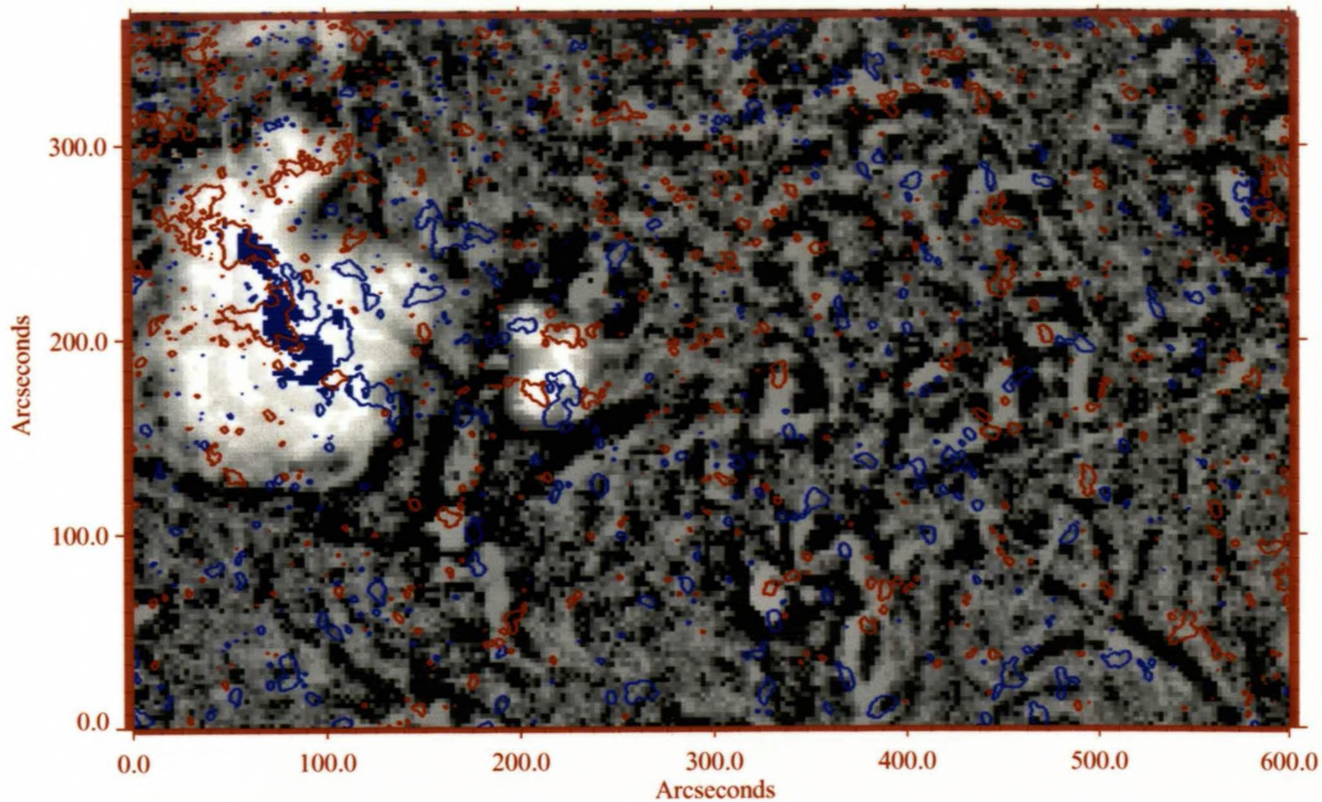

Figure 3.17: Fe XII coronal loops and the photospheric magnetic field. The EIT image is high-pass filtered as described in § 3.3. Red contours indicate −25 gauss, blue contours are +25 gauss. North is up and east is to the left; the image is dated 10-AUG-97 14:25:10 UT.

3.7.2 Emerging vs. Cancelling Bipoles

The MCC model currently does not account for the time evolution of coronal brightenings, but Longcope does anticipate one result of this future work. In the reconnection process, loops will not be heated and brighten until *after* they cross the separator. Hence, if magnetic loops are reconnecting across the separator (in the case of converging flux concentrations) they will fill with plasma and radiate after the current dissipation has occurred. These reconnected loops will lie just inside the separator as shown in figure 3.16, which is why the brightening is expected to be along the separator. In contrast, when bipoles are diverging, they will tend to reconnect to other distant concentrations. In this latter case, energy from the reconnection process will be deposited into loops elsewhere. This leads to an asymmetry in converging versus diverging bipoles, implying that emerging bipoles will not be observed in X-ray emission. The Parker model makes no statement on this issue and no bias towards merging vs. cancelling bipoles would be expected. Wave heating models similarly make no prediction.

We found numerous examples of emerging and cancelling regions associated with coronal brightenings. While we acknowledge previous studies that assert an inclination towards emerging or cancelling regions reconnecting in the corona (c.f. Webb et al. (1993) for a survey on this topic), we found no statistically significant bias in our data. As it is not necessary for magnetic concentrations to actually emerge or cancel for the MCC phenomena to be apparent, we also considered numerous examples of loops with footpoints passing each other on a closest approach trajectory. There was no clear bias in the observations.

3.8 Discussion

The observing campaign described in § 3.2.2 represents the longest high-cadence coordinated observation of the solar corona and photospheric magnetic field to date. The duration of the observation, the steady temporal cadence and the extent of the field of view have provided an unprecedented opportunity to study the entire lifetime of a variety of physical phenomena with signatures in both the photosphere and corona.

We find that the dimmest quiet sun coronal brightenings tend to be camouflaged by a diffuse background coronal haze present in the Fe XII images. When this haze (which varies slowly both spatially and temporally) is removed from the data with a spatial high-pass filter, the contrast of small-scale and other low-intensity loop structures is significantly enhanced. The resulting filtered images and movies show a very high level of coronal connectivity between photospheric flux concentrations, a much higher fraction than that observed by Harvey (1997) in soft X-ray images. A popular notion in the literature is that quiet sun regions in general have a much simpler topology than active regions. Careful study of the EIT/MDI movie, however, suggests these regions to be as complex as active regions, merely on a much smaller (and more difficult to observe) scale. The high resolution observations made possible by the MDI instrument (0.6 arcsecond pixels or 870 km resolution) show significant structure at the level of instrumental resolution. Preliminary findings by TRACE (A. M. Title and C. J. Schrijver 1998, private communication) similarly show unresolved flaring structures at the limiting resolution of that instrument (0.5 arcsecond pixels or 725 km). Qualitative observations from the EIT/MDI movie described in this paper show significant activity and structure on the smallest observable spatial scales evolving on timescales much faster than our temporal cadence.

From the high-pass filtered data we find that all photospheric flux concentrations $\gtrsim 3 \times 10^{18}$ Mx are associated with coronal brightenings visible in the EIT Fe XII (1.3 MK) channel. These observations are in near agreement with Schrijver et al. (1998), who found a similar threshold. We also find that emerging flux in quiet sun is never seen to expand to size scales typically associated with large-scale ($\gtrsim 15$ Mm) coronal loops. (The converse statement — large scale loops never converge and cancel against their own footpoints — also holds true.) What instead happens is a continuous process of discontinuous reconnection events: magnetic flux pairs emerge from the photosphere, spread and diffuse along the supergranular lanes, merge and/or cancel against other preexisting flux concentrations and the associated corona loops adjust accordingly. As the amount of flux present in a particular photospheric concentration increases, the range of distances within reach of that connection grows, and we find the maximum footpoint separations accessible to a bipole grows with increasing flux (c.f. figure 3.7). These bipoles may either connect to opposite-polarity concentrations of similar or greater strengths, or may connect to several concentrations at a range of possible distances. The pattern of connectivity also doesn't closely follow that of a potential magnetic field. Comparisons of potential vs. current-carrying loop structures (e.g., McClymont & Mikic 1994) show that the connectivity can vary dramatically depending on the presence of large-scale currents. Comparisons of potential field extrapolations from MDI magnetic fields to corresponding coronal images from EIT also do not fit the observations well (C. J. Schrijver 1997, private communication).

This last observation complicates other efforts at correlating the corona to events in the photosphere. Attempts to compare the typical scale size of coronal features (§ 3.5) to the magnetic field are frustrated by this issue of coronal loop connectivity. By direct measurement from the images we find typical small-scale brightenings with an average length of 18 Mm and via correlation methods the size scale is found to be somewhat larger at $\approx$ 26 Mm. The former approach is biased towards smaller, brighter features while the latter approach is biased in favor of large, bright structures which may explain the variation in size scales. Autocorrelation reveals other interesting features of the quiet corona: small-scale coronal loops in the quiet sun are isotropic in their orientation. It was anticipated that the loop orientation would tend to a predominently east-west orientation in accordance with Hale's Law (Hale 1919), but the results of the autocorrelation analysis does not support this view. It is observed that the typical scale size in the N-S and E-W directions is nominally the same in quiet sun. It is likely that these small-scale flux concentrations (often $\lesssim$ 2 Mm in size) are strongly influenced by the motions of the solar convective zone, while the large active region flux concentrations that are seen to obey this law are more resistant to being shifted about. Perhaps even more likely is the concept that even if the emerging flux were to emerge with a favored polarity orientation, the coronal reconnection events that follow within hours of emergence will most likely significantly alter the orientation of the coronal brightening. Isotropy in coronal brightening orientation is a natural consequence of (1) the moving, merging and cancellation of magnetic flux concentrations, and (2) the isotropic nature of the quiet sun photospheric magnetic field: concentrations uniformly separated by about the diameter of a supergranular cell will have little effect on the orientation of coronal loops once the process of reconnection sets in.

The EIT/MDI observations are also sufficient to consider several mechanisms of coronal heating. In § 3.7 we consider in some detail the predicted morphology of two methods of coronal heating and compare these predictions to observation. We suggest Alfvén wave heating and also describe the Parker Loop theory of twisting and braiding flux ropes as proxies for heating along the loop axis and the Longcope method of coronal heating along the separator as two independent methods of dispersing energy into the corona. The quiet sun observations presented here seem to agree very well with some form of either the Parker mechanism or wave heating: *all* flux concentrations above $\approx 3 \times 10^{18}$ Mx are associated with a coronal brightening, irregardless of relative motion, the orientation of the footpoint axis to the background magnetic field or other factors. Longcope's theory, however, suggests that for certain orientations of the the reconnecting magnetic bipole in relation to the background magnetic field, there will be no reconnection event (Longcope & Silva 1998). While others have observed this phenomena of separator heating (Kankelborg et al. 1996), we are unable to find unambiguous evidence of this happening in our dataset. Rough calculations suggest that on the size scales present in quiet sun, separator heating would be visible in approximately 15% of the loops reconnecting between magnetic footpoints. On the 17-minute cadence of the EIT observations, these heating events would likely only be visible for one frame and then disappear from the coronal images. We do not in general observe heating events like this with the appropriate morphology. Very preliminary results from the TRACE observatory at a much higher spatial resolution (0.5 arcsec pixel^{-1}) in comparison with MDI magnetograms do suggest evidence of possible separator heating (Schrijver 1998, private communication). It is conceivable that at the small spatial scales we consider here the modest EIT resolution of 2.59 arcsec pixel^{-1} is blurring the path of energy dissipation for these small coronal structures.

Returning to the Parker mechanism, there are numerous examples of bright coronal loops that must be subject to some form of continuous energy input. We do see isolated cases of loop structures that remain bright, but by the MCC method of heating should not be visible. Inspection of the photospheric footpoints suggest it is possible they may be undergoing a twisting motion of some fashion which would provide the necessary energy input, but it is not possible to resolve this sort of phenomena at the available spatial resolution. Parker (1988) suggested that magnetic observations on the order of 200 km (≈ 0.15 arcsecond pixels) would be necessary to see this twisting motion at the footpoints.

BIBLIOGRAPHY

BIBLIOGRAPHY

Acton, L. W. 1996, in Magnetodynamic Phenomena in the Solar Atmosphere — Prototypes of Stellar Magnetic Activity, ed. Y. Uchida, T. Kosugi, & H. Hudson (Kluwer), 3

Acton, L. W., Culhane, J. L., Gabriel, A. H., Bentley, R. D., Bowles, J. A., Firth, J. G., Finch, M. L., Gilbreth, C. W., Guttridge, P., Hayes, R. W., Joki, E. G., Jones, B. B., Kent, B. J., Leibacher, J. W., Nobles, R. A., Patrick, T. J., Phillips, K. J. H., Rapley, C. G., Sheather, P. H., Sherman, J. C., Stark, J. P., Springer, L. A., Turner, R. F., & Wolfson, C. J. 1980, Sol. Phys., 65, 53

Alexander, D., & Mackinnon, A. L. 1993, Sol. Phys., 144, 155

Antonucci, E. 1989, Sol. Phys., 121, 31

Blake, R. L., Chubb, T. A., Friedman, H., & Unzicker, A. E. 1963, ApJ, 137, 3

Brekke, P. 1993, ApJS, 87, 443

Brekke, P., & Kjeldseth-Moe, O. 1994, ApJ, 431, L55

Brekke, P., Rottman, G. J., Fontenla, J., & Judge, P. G. 1996, ApJ, 468, 418

Brueckner, G. E. 1981, Space Sci. Rev., 29, 407

Bruner, M. E., & McWhirter, R. W. P. 1988, ApJ, 326, 1002

Damè, L., Martic, M., Brown, W. A., Bruner, M. E., Strong, K., Suematsu, Y., Tsuneta, S., & Schmieder, B. 1996, Advances in Space Research, 17, 189

Deeg, H.-J., & Ninkov, Z. 1995, Op. Eng., 34, 43

Delaboudinière, J. P., Artzner, G. E., Brunaud, J., Gabriel, A. H., Hochedez, J. F., Millier, F., Song, X. Y., Au, B., Dere, K. P., Howard, R. A., Kreplin, R., Michels, D. J., Moses, J. D., Defise, J. M., Jamar, C., Rochus, P., Chauvineau, J. P., Marioge, J. P., Catura, R. C., Lemen, J. R., Shing, L., Stern, R. A., Gurman, J. B., Neupert, W. M., Maucherat, A., Clette, F., Cugnon, P., & Van Dessel, E. L. 1995, Sol. Phys., 162, 291

Deloach, A. C., Hagyard, M. J., Rabin, D., Moore, R. L., Smith, J., B. J., West, E. A., & Tandberg-Hanssen, E. 1984, Sol. Phys., 91, 235

Dere, K. P., Bartoe, J. D. F., & Brueckner, G. E. 1984, ApJ, 281, 870

Domingo, V., Fleck, B., & Poland, A. I. 1995, Sol. Phys., 162, 1

Dowdy, J., J. F., Rabin, D., & Moore, R. L. 1986, Sol. Phys., 105, 35

Doyle, J. G. 1996, A&A, 307, 162

Edlén, B. 1937, Zs. Ph., 104, 407

Falconer, D. A., Moore, R. L., Porter, J. G., Gary, G. A., & Shimizu, T. 1997, ApJ, 482, 519

Feldman, U., Doschek, G. A., & Mariska, J. T. 1979, ApJ, 229, 369

Fisher, G. H., Longcope, D. W., Metcalf, T. R., & Pevtsov, A. A. 1998, ApJ, in press.

Fontenla, J. M., Avrett, E. H., & Loeser, R. 1990, ApJ, 355, 700

Freeland, S. L., & Handy, B. H. 1998, Sol. Phys., in press.

Galsgaard, K., & Nordlund, Å. 1996, Astrophysical Letters & Communications, 34, 175

Golub, L. 1980, in Royal Society, Discussion on the Sun and the Heliosphere, April 3-4, 1980, 595

Golub, L., Krieger, A. S., Harvey, J. W., & Vaiana, G. S. 1977, Sol. Phys., 53, 111

Golub, L., Krieger, A. S., Silk, J. K., Timothy, A. F., & Vaiana, G. S. 1974, ApJ, 189, L93

Golub, L., Krieger, A. S., & Vaiana, G. S. 1976a, Sol. Phys., 49, 79

Golub, L., Krieger, A. S., & Vaiana, G. S. 1976b, Sol. Phys., 50, 311

Grotrian, W. 1939, Naturwissen., 27, 26

Hagenaar, H. J., Schrijver, C. J., & Title, A. M. 1997, ApJ, 481, 988

Hale, G. E. 1919, ApJ, 49, 153

Handy, B. H., Bruner, M. E., Tarbell, T. D., Title, A. M., Wolfson, C. J., Laforge, M. J., & Oliver, J. J. 1998, Sol. Phys., In press.

Harvey, K. L. 1997, in ASP Conference Series, Vol. 111, Proc. of Observations of Magnetic Reconnection in the Solar Atmosphere, held in Bath, England, March 20-22, 1996, 9

Harvey, K. L., Strong, K. T., Nitta, N., & Tsuneta, S. 1994, in Solar active region evolution: Comparing models with observations, ed. K. S. Balasubramaniam & G. W. Simon (A.S.P.), 377

Harvey-Angle, K. L. 1993, Ph.D. thesis, Sterrekundig Instituut, Universiteit Utrecht

Hawley, S. L., & Fisher, G. H. 1994, ApJ, 426, 387

Kankelborg, C. C., Walker, I., Arthur B. C., Hoover, R. B., & Barbee, J., Troy W. 1996, ApJ, 466, 529

Kendall, M. G., & Moran, P. A. P. 1963, Geometrical Probability, Griffin's Statistical Monographs & Courses No. 10 (Charles Griffin & Company Limited)

Klimchuk, J. A. 1992, in ESA, Proceedings of the First SOHO Workshop: Coronal Streamers, Coronal Loops, and Coronal and Solar Wind Composition, 167

Kopp, R. A., & Kuperus, M. 1968, Sol. Phys., 4, 212

Kristianpoller, N., & Dutton, D. 1964, Appl. Opt., 3, 287

Lean, J., Vanhoosier, M. E., Brueckner, G., Prinz, D., Floyd, L., & Edlow, K. 1992, Geophys. Res. Lett., 19, 2203

Leighton, R. B., Noyes, R. W., & Simon, G. W. 1962, ApJ, 135, 474

Litwin, C., & Rosner, R. 1998, ApJ, 499, 945

Longcope, D. W. 1996, Sol. Phys., 169, 91

Longcope, D. W. 1998, ApJ, 507, to appear.

Longcope, D. W., & Silva, A. V. R. 1998, Sol. Phys., 179, 349

Macleod, H. A. 1986, Thin-Film Optical Filters (Macmillan Publishing Co.)

Mariska, J. T. 1992, The Solar Transition Region, Cambridge Astrophysics Series No. 23 (Cambridge University Press)

McClymont, A. N., & Mikic, Z. 1994, ApJ, 422, 899

McKenzie, D. E., & Mullan, D. J. 1997, Sol. Phys., 176, 127

Metcalf, T. R., Canfield, R. C., Hudson, H. S., Mickey, D. L., Wulser, J. P., Martens, P. C. H., & Tsuneta, S. 1994, ApJ, 428, 860

Mosher, J. M. 1977, Ph.D. thesis, California Inst. of Tech., Pasadena.

Narain, U., & Ulmschneider, P. 1996, Space Sci. Rev., 75, 453

Parker, E. 1983a, ApJ, 264, 635

Parker, E. 1983b, ApJ, 264, 642

Parker, E. N. 1988, ApJ, 330, 474

Pierce, A. K., & Allen, R. G. 1977, in The Solar Output and its Variation, ed. O. R. White (Colorado University Press), Ch. IV, 169

Press, W. H., Teukolsky, S. A., Vetterling, W. T., & Flannery, B. P. 1992, Numerical Recipes in FORTRAN (2nd ed.) (Cambridge University Press)

Reeves, E. M., Noyes, R. W., & Withbroe, G. L. 1972, Sol. Phys., 27, 251

Rosner, R., Tucker, W. H., & Vaiana, G. S. 1978, ApJ, 220, 643

Rottman, G. J., Woods, T. N., & Sparn, T. P. 1993, J. Geophys. Res., 98, 10667

Scherrer, P. H., Bogart, R. S., Bush, R. I., Hoeksema, J. T., Kosovichev, A. G., Schou, J., Rosenberg, W., Springer, L., Tarbell, T. D., Title, A., Wolfson, C. J., Zayer, I., & The MDI Engineering Team. 1995, Sol. Phys., 162, 129

Schrijver, C. J. 1987, A&A, 180, 241

Schrijver, C. J. 1990, in Mechanisms of Chromospheric and Coronal Heating — Proceedings of the International Conference, Heidelberg, 5-8 June 1990, ed. P. Ulmschneider, E. R. Priest, & R. Rosner (Springer-Verlag), 257

Schrijver, C. J., Shine, R. A., Hurlburt, N. E., Tarbell, T. D., & Lemen, J. R. 1998, in Proceedings of the Fifth SoHO Workshop — The Corona and Solar Wind near Minimum Activity 17-20 June 1997, 669

Schrijver, C. J., Title, A. M., Van Ballegooijen, A. A., Hagenaar, H. J., & Shine, R. A. 1997, ApJ, 487, 424

Simon, G. W., & Leighton, R. B. 1964, ApJ, 140, 1120

Stix, M. 1989, The Sun, Astronomy and Astrophysics Library (Springer-Verlag)

Strong, K. T., Harvey, K., Hirayama, T., Nitta, N., Shimizu, T., & Tsuneta, S. 1992, PASJ, 44, L161

Tandberg-Hanssen, E., Cheng, C. C., Woodgate, B. E., Brandt, J. C., Chapman, R. D., Athay, R. G., Beckers, J. M., Bruner, E. C., Gurman, J. B., & Hyder, C. L. 1981, Adv. Space Res., 1, 275

Tarbell, T. D., Bruner, M., Jurcevich, B., Lemen, J., Strong, K., Title, A., Wolfson, J., Golub, L., & Fisher, R. 1994, in Proc. of the Third SoHO Workshop — Solar Dynamic Phenomena and Solar Wind Consequences 26–29 September 1994, 375

Title, A., Bruner, M., Jurcevich, B., Lemen, J., Strong, K., Tarbell, T., Wolfson, J., Golub, L., & Fisher, R. 1995, Bull. Am. Astron. Soc., 187, 10107

Tsuneta, S., Acton, L., Bruner, M., Lemen, J., Brown, W., Carvalho, R., Catura, R., Freeland, S., Jurcevich, B., Morrison, M., Ogawara, Y., Hirayama, T., & Owens, J. 1991, Sol. Phys., 136, 37

Vaiana, G. S., Van Speybroeck, L., Zombeck, M. V., Krieger, A. S., Silk, J. K., & Timothy, A. 1977, Space Science Instrumentation, 3, 19

Vernazza, J. E., Avrett, E. H., & Loeser, R. 1981, ApJS, 45, 635

Webb, D. F., Martin, S. F., Moses, D., & Harvey, J. W. 1993, Sol. Phys., 144, 15

Wilhelm, K., Curdt, W., Marsch, E., Schuhle, U., Lemaire, P., Gabriel, A., Vial, J. C., Grewing, M., Huber, M. C. E., Jordan, S. D., Poland, A. I., Thomas, R. J., Kuhne, M., Timothy, J. G., Hassler, D. M., & Siegmund, O. H. W. 1995, Sol. Phys., 162, 189

Woodgate, B. E., Tandberg-Hanssen, E. A., Bruner, E. C., Beckers, J. M., Brandt, J. C., Henze, W., Hyder, C. L., Kalet, M. W., Kenny, P. J., Knox, E. D., Michalitsianos, A. G., Rehse, R., Shine, R. A., & Tinsley, H. D. 1980, Sol. Phys., 65, 73

Zwaan, C., & Schrijver, C. J. 1999, Magnetic activity in Sun and stars (Cambridge University Press), in preparation.